Target Single Spin Asymmetry in Semi-Inclusive Deep-Inelastic $(e, e'\pi^{\pm})$ Reaction on a Transversely Polarized Proton Target

July 5, 2011

(A new proposal to JLab-PAC38)

A. Kolarkar
Boston University, Boston, MA

X. Qian
California Institute of Technology, Pasadena, CA

K. Aniol, D. J. Margaziotis
California State University-Los Angles, Los Angles, CA

X.Z. Bai, H.X. He, S.Y. Hu,
X.M. Li, H.H. Xia, J. Yuan, J. Zhou, S.H. Zhou
China Institute of Atomic Energy, Beijing, P. R. China

D. Armstrong, T. Averett, P. Bradshaw, B. Zhao
College of William & Mary, Williamburg, VA

H. Gao (Spokesperson/Contact), M. Huang, G. Laskaris,
S. Malace, M. Meziane, C. Peng, Q.J. Ye, Y. Zhang, W.Z. Zheng
Duke University and TUNL, Durham, NC

P. Markowitz, L. Guo
Florida International University, Miami, FL

Y. Li, L.Y. Zhu
Hampton University, Hampton, VA

H.P. Cheng, R.C. Liu, H.J. Lu, Y. Shi
Huangshan University, Huangshan, P. R. China

X.S. Chen, N. Li
Huazhong University of Science and Technology, Wuhan, P. R. China

U. D'Alesio, F. Murgia
Cagliari University and INFN, Cagliari Torino, Italy

R. De Leo, L. Lagamba, S. Marrone, G. Simonetti, I. Vilardi
INFN-Bari and University of Bari, Bari, Italy

L. Barion, M. Contalbrigo, C. Giuseppe, P. Lenisa, L. L. Pappalardo
University of Ferrara and INFN Ferrara, Ferrara, Italy

M. Aghasyan, E. De Sanctis, D. Hasch,
M. Mirazita, S. A. Pereira, S. Pisano, P. Rossi
INFN Laboratori Nazionali di Frascati, Frascati, Italy

A. Bacchetta, B. Pasquini
INFN, Sezione di Pavia, Pavia, Italy

S. Scopetta
University degi Studi di Perguria, INFN, Perugia, Italy

E. Pace
Rome-Tor Vergata University, Rome, Italy

E. Cisbani, F. Cusanno, S. Frullani, F. Garibaldi,
F. Meddi, G. Salme', G. M. Urciuoli
INFN-Roma and gruppo collegato Sanitá, Rome, Italy

M. Anselmino, M. Boglione
Torino University and INFN, Torino, Italy

A. Afanasev, K. Allada (Spokesperson), A. Camsonne,
J.-P. Chen (Spokesperson), E. Chudakov, A. Deur, J. Gomez,
D. W. Higinbotham, J. O. Hansen, C. W. de Jager, M. Jones, J. LeRose,
R. Michaels, S. Nanda, A. Prokudin, Y. Qiang, M. Schlegel,
B. Sawatzky, B. Wojtsekhowski, J. Zhang
Jefferson Lab, Newport News, VA

M. Mihovilovič, S. Širca
Jožef Stefan Institute, Liubljana, Slovenia

B.T. Hu, Y. Zhang
Lanzhou University, Lanzhou, P. R. China

F. Yuan
Lawrence Berkeley National Laboratory, Berkeley, CA

T. Holmstrom
Longwood University, Farmville, VA

X. Jiang, M.X. Liu, A. Puckett
Los Alamos National Laboratory, Los Alamos, NM

W. Bertozzi, S. Gilad, J. Huang, A. Kelleher, N. Muangma,
K. Pan, V. Sulkosky
Massachusetts Institute of Technology, Cambridge, MA

J. Dunne and D. Dutta
Mississippi State University, Starkville, MS

M. Burkardt
New Mexico State University, Las Cruces, NM

L. Weinstein
Old Dominion University, Norfolk, VA

B.-Q. Ma, Y.J. Mao
School of Physics, Peking University, P. R. China

L. Gamberg
Pennsylvania State University at Berks, Reading, PA

B. Xiao
Pennsylvania State University, University Park, PA

L. El Fassi, R. Gilman, G. Kumbartzki,
R. Ransome, Y.W. Zhang
Rutgers University, Piscataway, NJ

Seonho Choi, Hoyoung Kang, Hyekoo Kang,
Byungwuek Lee, Yoomin Oh
Seoul National University, Seoul, Korea

Z.T. Liang, X.T. Huang
Shangdong University, Jinan, China

A. J. Sarty
St. Mary's University, Halifax, Nova Scotia, Canada

P. Souder and R. Holmes
Syracuse University, Syracuse, NY

E. Piasetzky
Tel aviv University, Tel Aviv, Israel

W. Armstrong, D. Flay, E. Fuckey, Z.-E. Meziani (Spokesperson),
M. Posik, E Schulte, N. Sparveris, H. Yao
Temple University, Philadelphia, PA

W.-C. Ding, Y.L. Li, J.-B. Wang, Y. Wang, Z.G. Xiao
Tsinghua University, Beijing, P. R. China

P. Schweitzer
University of Connecticut, Storrs, CT

J. Annand, D. Hamilton, D. Ireland, K. Livingston, R. Kaiser,
I.J.D. MacGregor, D. Protopopescu, G. Rosner, B. Seitz
University of Glasgow, Glasgow, Scotland

A. Nathan, N. Makins, J.-C. Peng
University of Illinois, Urbana-Champaign, IL

W. Korsch
University of Kentucky, Lexington, KY

E.J. Beise
University of Maryland, College Park, MD

K. Kumar, S. Riordan
University of Massachusetts, Amherst, MA

C. Dutta
University of Michigan, Ann Arbor, MI

T. Badman, J. Maxwell, S. Phillips, K. Slifer, R. Zielinski
University of New Hampshire, Durham, NH

L. Gan
University of North Carolina, Wilmington, NC

K. Hu, M. Shao, X.L. Wang, Z.Z. Xu, X. Yan, W.B. Yan,
Y. Ye, Y.X. Zhao, Z.G. Zhao, Z.Y. Zhang, P.J. Zhu
University of Science and Technology of China, Hefei, P. R. China

H. Baghdasaryan, G. Cates, D. Crabb, M. Dalton, D. Day,
N. Kalantarians, R. Lindgren, N. Liyanage, V. Nelyubin, B. Norum, K. Paschke,
M. H. Shabestari, W. A. Tobias,
K. Wang, Z. W. Zhao, X.C. Zheng
University of Virginia, Charlottesville, VA

and the HallA Collaboration

Abstract

We propose to carry out measurements of Single target Spin Asymmetries (SSA) from semi-inclusive electroproduction of charged pions from a transversely polarized NH_3 target in Deep-Inelastic-Scattering kinematics using 11 and 8.8 GeV electron beams. This coincidence experiment will be carried out in Hall A with the approved large acceptance solenoid spectrometer (SoLID). Large azimuthal angular coverages on ϕ_h and ϕ_S angles are important in controlling systematic uncertainties in extracting different asymmetries. The proposed experiment will provide 4-D (x, z, P_T and Q^2) data on the Collins, Sivers and Pretzelosity asymmetries for the proton through the azimuthal angular dependence of the outgoing hadron relative to target spin. The results from this experiment, when combined with the approved SoLID neutron (^{3}He) Collins asymmetry measurement and the Collins fragmentation function determined from the e^+e^- collision data, will allow for a flavor separation of the quark tensor charge, and achieve a determination of the tensor charge of u/d quark to better than 10% accuracy. The extracted Sivers and Pretzelosity asymmetries will provide important information to understand the quark orbital motion and the nucleon/quark spin correlations. We request a total of 120 days of beam time (polarized) at incident beam energies of 11 and 8.8 GeV and at a beam current of 100 nA.

Contents

1 Introduction

Understanding the internal structure of nucleon and nucleus in terms of quarks and gluons, the fundamental degrees of freedom of Quantum Chromodynamics (QCD), has been and still is the frontier of subatomic physics research. QCD as a theory of the strong interaction has been well-tested by observables with a large momentum transfer in high energy experiments. Our knowledge on the universal parton distribution functions (PDFs) and fragmentation functions (FFs), which connect the partonic dynamics to the observed hadrons, has been dramatically improved in recent years [1]. As a probability density to find a parton (quark or gluon) inside a hadron with the parton carrying the hadron's longitudinal momentum fraction x, the PDFs have provided us with the nontrivial and quantitative information about the partonic structure of a hadron.

In recent years, the hadronic physics community has extended its investigation of partonic structure of hadrons beyond the PDFs by exploring the parton's motion and its spatial distribution in the direction perpendicular to the parent hadron's momentum. Such effort is closely connected to the study and extraction of two new types of parton distributions: the transverse momentum dependent parton distributions (TMDs) [2, 3, 4, 5, 6, 7, 8, 9], and the generalized parton distributions (GPDs) [8, 10, 11, 12, 13, 14, 15, 16]. The ultimate knowledge of finding a single parton inside a hadron – involving both momentum and space information – could be encoded in the phase-space distributions of quantum mechanics, such as the Wigner distribution $W(\vec{k}, \vec{b})$,whose integration over the parton spatial dependence ($\vec{b}$) leads to the TMDs, while its integration over transverse momentum ($\vec{k}$) provides the parton's spatial distribution that is relevant to the GPDs. A quantum field theory version of the phase-space distributions, in terms of the matrix element of the Wigner operator, was discussed in Ref. [17]. Understanding both the momentum and spatial distributions of a parton inside a hadron in terms of the more general Wigner distributions could be the central object of future studies on partonic structure. Knowledge of TMDs is also crucial for understanding some novel phenomena in high energy hadronic scattering processes, such as, the single transverse spin asymmetries [18, 19, 20, 21, 22, 23, 24] and small-x saturation phenomena [25, 26, 27, 28, 29, 30, 31, 32].

Like the PDFs, the TMDs and GPDs carry rich information on hadron's partonic structure, while they are not direct physical observables due to the color confinement of QCD dynamics. It is the leading power QCD collinear factorization theorem [33] that connects the PDFs to the hadronic cross sections with large momentum transfers: Q's $\gg \Lambda_{\rm QCD}$. In order to study the TMDs, we need the corresponding TMD factorization theorem for physical observables that are sensitive to parton's transverse motion and the TMDs. Such observables often involve two very different momentum scales: $Q_1 \gg Q_2 \gtrsim \Lambda_{\rm QCD}$, where the large Q_1 is necessary to ensure any perturbative QCD calculation while the small scale Q_2 is needed so that these observables are sensitive to the parton's transverse motion. The transverse momentum distribution of single hadron production in semi-inclusive deep inelastic lepton-hadron scattering (SIDIS) and Drell-Yan lepton pair production in hadronic collisions are two natural examples. The TMD factorization for these two processes have been carefully examined [34, 35, 36]. However, the TMD factorization in QCD is much more restrictive than the leading power collinear factorization. The conventional TMD factorization works for three-types of observables with only two identified hadrons:

single hadron p_T distribution in SIDIS, the p_T distribution of Drell-Yan type process, and two-hadron momentum imbalance in e^+e^- collisions. But it has been shown to fail for observables with more than two identified hadrons [37, 38, 39, 40, 41].

Important aspects of the TMD parton distributions, such as the gauge invariance, the role of gauge links, and the universality, have been explored in recent years [20, 21, 22, 23, 24, 42, 43, 44]. Like the PDFs, the definition of TMDs is closely connected to the factorization of physical cross sections, and it is necessary for the TMDs to include all leading power long-distance contributions to the physical cross sections if they could be factorized. All leading power collinear gluon interactions are summed into the gauge links in the definition of the TMDs. It is the gauge link that makes the TMDs gauge invariant and provides the necessary phase for generating a sizable single transverse spin asymmetry (SSA) in SIDIS and Drell-Yan processes [18, 19, 20, 21, 22, 23]. However, unlike the PDFs, which are universal, the TMDs could be process dependent due to the fact that the initial-state and final-state collinear gluon interactions are summed into two different gauge links. That is, the TMDs extracted from SIDIS could be different from those extracted from Drell-Yan processes because of the difference in gauge links. Although the TMDs are not in general universal, it could be shown from the parity and time-reversal invariance of QCD dynamics that the process dependence of the spin-averaged as well as spin-dependent TMDs is only a sign, which was referred to as the parity and time-reversal modified universality [20, 24]. An important example of the modified universality is that the Sivers function extracted from the SIDIS measurements is opposite in sign from the Sivers function extracted from the Drell-Yan process. The test of the sign change of the Sivers function from SIDIS to Drell-Yan is a critical test of the TMD factorization.

TMDs provide new, fundamental information about the structure of the nucleon by imaging its partonic structure, dynamics, and spin-orbital couplings in three-momentum space. At leading twist there are eight TMD quark distributions [9]: three of them, the unpolarized, the helicity and the transversity distributions, survive in the collinear limit, while the other five vanish in such a limit. All eight TMDs are categorized in fig. 1 by the nucleon and parton spin information. Each TMD quark distribution explores one unique feature of the quark inside a polarized or unpolarized nucleon. An intuitive interpretation of the transversity distribution, h_1, is that it gives the probability of finding a transversely polarized parton inside a transversely polarized nucleon with certain longitudinal momentum fraction x and certain transverse momentum k_T. The Sivers function [3, 45],$f_{1T}^{\perp}$, provides the number density of unpolarized partons inside a transversely polarized proton, while the Boer-Mulders function [6], $h_1^{\perp}$, gives the number density of transversely polarized quarks inside an unpolarized proton. Both the Sivers function $f_{1T}^{\perp}$ and the Boer Mulders function $h_1^{\perp}$ require wave function components with nonzero orbital angular momentum and thus provide information about the correlation between the quark orbital angular momentum (OAM) and the nucleon/quark spin, respectively. Furthermore, they are (naive) T-odd functions which rely on the final state interactions (FSI) experienced by the active quark in a SIDIS experiment as both functions vanish without FSI. Although FSIs are usually unwelcome phenomena because they tend to be inextricably intertwined with the structure information one is interested in, they also provide important information of QCD. The Sivers and Boer-Mulders function provide a

clean probe of the QCD FSI. In contrast to $f_{1T}^{\perp}$ and $h_1^{\perp}$, the functions g_{1T} and $h_{1L}^{\perp}$ are (naive) T-even, and thus do not require FSI to be nonzero. Nevertheless, they also require interference between wave function components that differ by one unit of OAM and thus require OAM to be nonzero. Finally, the 'pretzelosity' $h_{1T}^{\perp}$ requires interference between wave function components that differ by two units of OAM (e.g. p-p or s-d interference). Combining the wealth of information from all these functions could thus be invaluable for disentangling the spin orbit correlations in the nucleon wave function, thus providing important information about the quark orbital angular momentum, and for imaging of the nucleon in full momentum space.

Because of the importance of the parton transverse momentum in fully understanding the nucleon structure and the QCD dynamics, the field of TMD is rapidly growing and major theoretical progresses have been made in the last a couple of years both in lattice QCD calculations and in various quark models. Recently, the first numerical results on T-even, "process-independent" TMDs were reported [46, 47] on the lattice. These calculations are performed with the direct, straight gauge link between the quark fields ("process-independent"), as such at the present time they can not be compared with those from experimental mesurements of SIDIS and Drell-Yan processes. However, these first lattice QCD calculations represent major advancements in the study of TMD physics. In principle, calculations on the lattice relevant to SIDIS or Drell-Yan processes could be feasible if one can create a staplelike gauge link, but major technical challenges need to be overcome such as handling diminishing signal-to-noise ratios for increasing nucleon momenta and the statistical noise created by the long gauge link. At the DIS2011 workshop, preliminary results on Sivers and Boer-Mulders functions were reported [48] using a staplelike gauge link.

Although explicit gluon degrees of freedom are lacking in quark models, major progresses have been made utilizing quark models in gaining insight about TMDs and providing tools for analyzing SIDIS and Drell-Yan data in a phenomenolgical way. We do not attempt to review the entire area of quark model studies of TMDs, rather we discuss briefly few of them.

Recently, a study of six leading-twist and eight subleading-twist TMDs (14 $T-$ even TMDs in total) in the bag model were reported [49] . This is the first paper in which twist-3 TMDs in a quark model are presented and the authors have shown that there are 9 linear and 2 nonlinear relations among these 14 T-even leading and subleading-twist TMDs. One of those linear relations connects the moment of pretzelosity to the difference of g_1^q and h_1^q. Such a difference between the helicity and transversity distributions is found to be related to quark orbital angular momentum (OAM) in a light-cone SU(6) quark-diquark model [50, 51], and provides a connection of a TMD (pretzelosity distribution) to OAM in a model dependent way beyond the intuitive picture that TMDs are connected to OAM [49],

$$L_q^3 = (-1) \int dx h_{1T}^{\perp(1)q}(x)$$

This finding also agrees with that from a light-cone SU(6) quark-diquark model [52] at leading twist. Another finding of [49], which is important to the phenomenology of TMDs, concerns the factorization of x and p_T in TMDs. Often a Gaussian form has been assumed for the p_T dependence. In the valence quark region, the effective Gaussian Ansatz

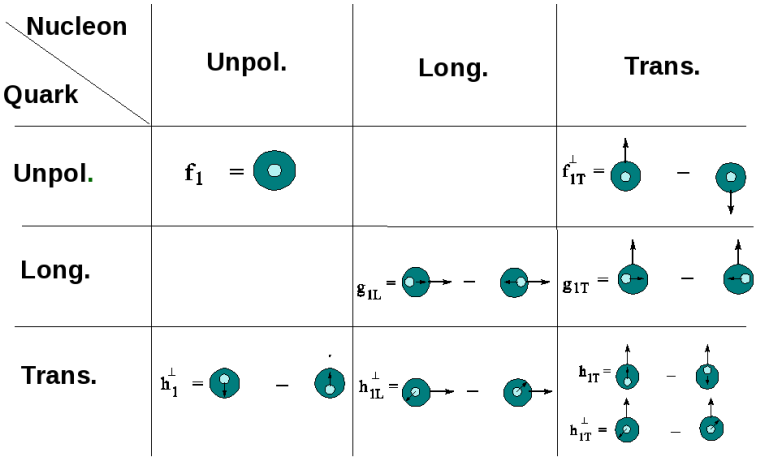

Figure 1: All eight TMDs at leading twist are categorized by the nucleon and parton spin information.

approximates reasonably well the extracted results from the model up to $p_T \leq O(M_N)$. For a comprehensive discussion of various quark models, linear and nonlinear, flavor-dependent and independent relationships of various TMDs at twist two, we refer to a recent paper [53].

Most recently, five-dimensional Wigner functions in transverse position and three-momentum of the quark relative to the nucleon are studied [54]. The Wigner functions are obtained by Fourier transform in the transverse space of the generalized transverse-momentum dependent parton distributions [55]. Quark OAMs are then calculated using these Wiger functions within different light-cone quark models and the results are compared to different definitions of OAM using generalized parton distributions and TMDs. While results for individual quark flavor are different using different OAM definitions, the sum of quark OAM is found to be the same using all three definitions.

In the experimental front, although we have gained a lot of information on the collinear PDFs and helicity distributions, we know very little about quark's and gluon's intrinsic transverse motion inside a nucleon. Recent measurements of multiplicities and double spin asymmetries as a function of the final transverse momentum of pions in SIDIS at JLab [56, 57] suggest that transverse momentum distributions may depend on the polarization of quarks and possibly also on their flavor. Calculations of transverse momentum dependence of TMDs in different models [58, 59, 60, 61] and on lattice [46, 47] indicate that dependence of transverse momentum distributions on the quark polarization and flavor may be very significant. The recent discovery of a "sign mismatch" [62] between the Sivers function and the corresponding twist-three quark-gluon correlation function $T_{q,F}(x,x)$ extracted from SIDIS and single hadron production from pp collision highlights further the importance of new, precision data in multi-dimensions of the phase space. Therefore, experiments with both polarized "neutron" and proton targets using the same experimental apparatus with a wide kinematic coverage for all four important kinematic variables (x, z, P_T, Q^2) of SIDIS are crucial.

2 The Phenomenology SSAs and TMDs

All eight leading twist TMDs can be accessed in SIDIS. Four of them (transversity, sivers, pretzelosity and g_{1T}) can be accessed through a transversely polarized target. There are three mechanisms which can lead to the Single (transversely polarized target) Spin azimuthal Asymmetry (SSA) for semi-inclusive DIS electroproduction of pions. They are the so-called Collins asymmetry, the Sivers asymmetry and the Pretzelosity asymmetry. The quark transversity function in combination with the chiral-odd Collins fragmentation function [63] gives rise to an azimuthal (Collins) asymmetry in $sin(\phi_h + \phi_S)$, where azimuthal angles of both the hadron (pion) (ϕ_h) and the target spin (ϕ_S) are about the virtual photon axis and relative to the lepton scattering plane. The Sivers asymmetry [3, 64, 65] refers to the azimuthal asymmetry in $sin(\phi_h - \phi_S)$ due to the correlation between the transverse target polarization of the nucleon and the transverse momentum of the quarks, which involves the orbital angular momentum of the unpolarized quarks [18, 66]. The Pretzelosity asymmetry is similar to Collins asymmetry except the polarization is due to quarks polarized perpendicularly to the nucleon spin direction in the transverse plane inside a transversely polarized nucleon. It has an azimuthal angular dependence of $sin(3\phi_h - \phi_S)$. One can disentangle these angular distributions by taking the azimuthal moments of the asymmetries as has been done by the HERMES Collaboration [67] and the COMPASS Collaboration [68]. Studying SSA on transversely polarized target with longitudinally polarized beam can give access to g_{1T} in $< \cos(\Phi_h - \Phi_S) >$ azimuthal modulation, g_{1T} being T-even couples to unpolarized fragmentation function D_1. Another interesting opportunity is the study of $< \cos 2\Phi_h >$ azimuthal modulation of unpolarized cross section that is due to Boer-Mulders function $h_1^\perp$ that describes transversely polarized quarks in an unpolarized hadron and couples to Collins fragmentation function $H_1^\perp$.

In recent years a great deal of understanding of transverse spin effects, final state interactions, and the spin orbit structure of partonic-hadronic interactions has been gained from model calculations of the TMDs and fragmentation functions. In particular the final state interactions in TSSAs through the Sivers function has been studied in spectator models and the light-cone wave function approach [18, 21, 58, 69, 70, 71, 72, 73] as well as the bag model [74]. The Collins function has been calculated in [75, 76] while studies of the universality of T-odd fragmentation functions have been carried out in [36, 77, 78]. The Boer-Mulders function has been calculated in [79, 69, 80, 71, 73] and the spin orbit effects of the pretzelosity function have been studied in both light-cone constituent quarks models [81, 52, 82, 83], while model predictions of azimuthal and transverse spin asymmetries have been predicted in [71, 84, 85].

Among the TMDs vanishing in the collinear limit, the Sivers function is the best known and has been phenomenologically extracted by several groups mainly from analyzing the azimuthal distribution of a single hadron in SIDIS [86, 87, 88, 89, 90]. The extracted Sivers functions from [90] are shown in Fig. 2. However, in the case of positive hadrons, where a signal has been seen, the measurements of HERMES [91] and COMPASS [92] experiments are only marginally compatible: the asymmetries measured by COMPASS are somewhat smaller, and seem to indicate an unexpected dependence on W, the mass of the hadronic final state. The first model dependent extractions of the transversity distribution have been carried out [93] by combining SIDIS [67, 91, 94, 95] data with

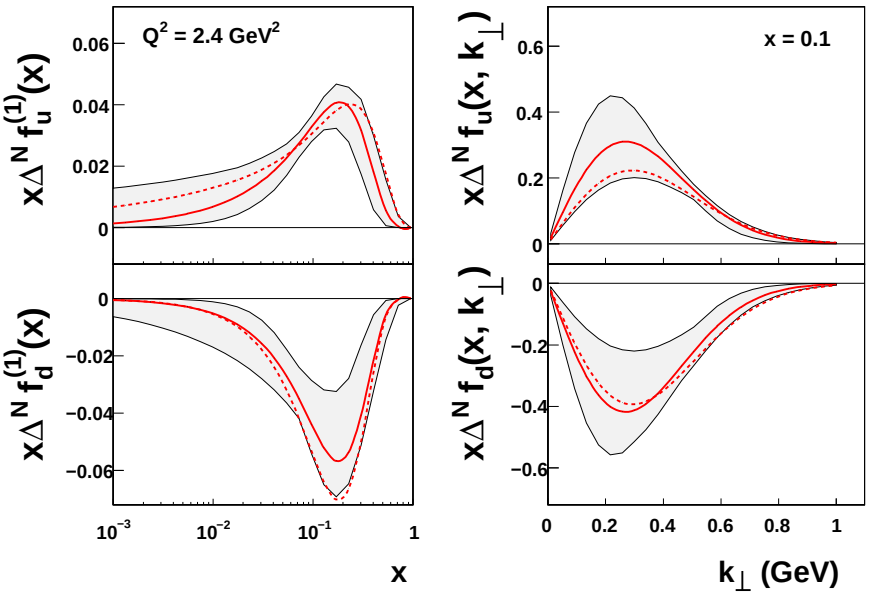

Figure 2: From [90], the Sivers distribution functions for u and d flavors, at the scale $Q^2 = 2.4$ (GeV/c)^2, as determined by an updated model-dependent fit (solid lines) are compared with those of an earlier fit [86] of SIDIS data (dashed lines), where π^0 and kaon productions were not considered and only valence quark contributions were taken into account. This plot shows that the Sivers functions previously found are consistent, within the statistical uncertainty bands, with the Sivers functions obtained in [90].

e^+e^- data [96] on the Collins function (see Figure 3). Within the uncertainties, the Soffer bound is respected.

Complementing the data from the HERMES [67, 91], COMPASS [95], and BELLE [96] experiments, the recent release from the Jefferson Lab HallA experiment E06-010 [99] on the neutron (with polarized ^{3}He) will facilitate a flavor decomposition of the transversity distribution function, h_1 [100, 101] and the Sivers distribution function $f_{1T}^{\perp}$ [3] in the overlapping kinematic region. The extracted neutron Collins/Sivers moments from [99] are shown in Fig. 4. The Collins moments are compared with the predictions based on phenomenological fits of other data [93], a light-cone quark model calculation [60, 102] and quark-diquark model [83, 103] calculations. The phenomenological fit and the model calculations, which assume Soffer's bound [98], predict rather small Collins asymmetries which are mostly consistent with the data shown in fig. 4. However, the π^+ Collins moment at $x = 0.34$ is suggestive of a noticeably more negative value at the 2σ level. These new neutron data favor negative π^+ Sivers moments, while the π^- moments are close to zero. Such behavior independently supports a negative d quark Sivers function, which has been suggested by the phenomenological fit [86, 104] to HERMES and COMPASS data, a light-cone quark model calculation [105, 106], and an axial diquark model calculation[107]. In

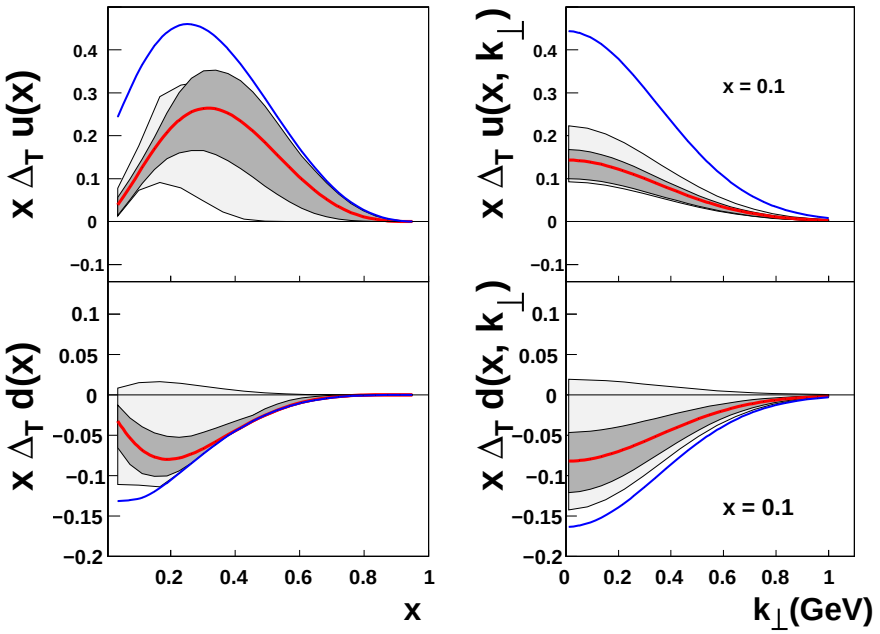

Figure 3: From [97], the transversity distribution functions for u and d flavors as determined by a global fit analysis, at $Q^2 = 2.4$ GeV^2 [97]. The Soffer bound [98] (highest or lowest lines) and the (wider) uncertainty bands of a previous extraction [93] are displayed.

addition, the central values of these new data are slightly smaller in magnitude than the phenomenological fit.

Information on the rest of the TMDs is rather scarce. Nevertheless, these recent results have already generated great excitement, which is evident from the increasingly active theoretical activities, including modeling [53] and lattice QCD calculations [46, 47, 48], and planning of future experiments [1]. However, a model-independent determination of these leading twist functions requires data in a wider kinematic range with high precision in *four dimensions* (Q^2, x, z, P_T). Recently, a new experiment [108, 109, 110] with an 11-Gev electron beam, a high-pressure polarized ^{3}He target, and a solenoid detection system (SoLID) [111] has been approved. This new experiment will provide data on the neutron with very high statistical accuracy and excellent systematic precision. over a Q^2 range of 1 - 8 (GeV/c)^2 and a large range of x, z, and P_T values. Another SoLID proposal [112] has been approved in which asymmetries in semi-inclusive deep-inelastic electroproduction of charged pions on a longitidinally polarized ^{3}He target at 8.8 and 11 GeV will be measured. In this proposal, the main focus is to measure the Collins, Sivers and Pretzelosity SSAs with an unpolarized beam and a transversely polarized proton target. This new experiment together with previously approved neutron experiment (^{3}He target) will not only provide precise determination of the Collins, Sivers and pretzelosity asymmetries from neutron and proton, but also allow for a flavor separation of TMDs,

[1] COMPASS II and new experiments discussed in this proposal.

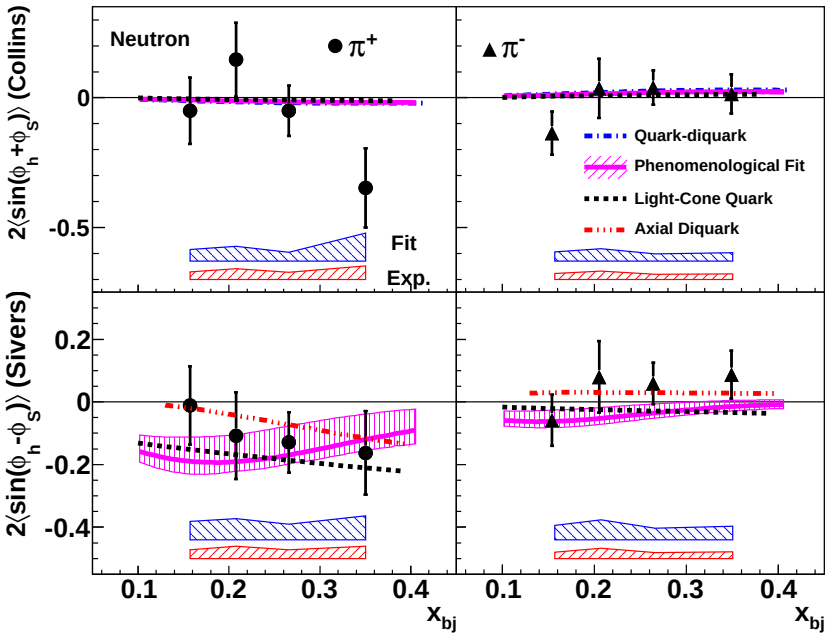

Figure 4: The extracted neutron Collins and Sivers moments with uncertainty bands for both π^+ and π^- electro-production. For details, see Ref. [99].

which is very important to test theoretical predictions of TMDs and to improve our understanding of QCD. In particular, the results from this experiment, when combined with the approved SoLID neutron (^{3}He) Collins asymmetry measurement and the Collins fragmentation function determined from the e^+e^- collision data, will allow for a flavor separation of the quark tensor charge, and achieve a determination of the tensor charge of u/d quark to better than 10% accuracy. Such an accuracy is essential for testing lattice QCD predictions which are becoming more precise.

3 Formalism for SIDIS

3.1 Transverse target spin related SIDIS cross sections

The differential cross section in a SIDIS $(e, e'h)$ reaction, in which the beam is not polarized and the target is transversely polarized, can be expressed as the sum of target spin-independent and target spin-dependent terms at leading twist:

$$\begin{aligned} \frac{d\sigma^h}{dx_B dy d\phi_S dz_h d\phi_h dP_{h\perp}^2} \equiv d\sigma^h &= d\sigma_{UU} + d\sigma_{UT}, \\ &= d\sigma_{UU} + d\sigma_{UT}^{Collins} + d\sigma_{UT}^{Sivers} + d\sigma_{UT}^{Pretzelosity} \end{aligned} \tag{1}$$

Each term in Eq. 1 can be expressed as convolutions of transverse momentum dependent parton distribution functions (TMDs) and fragmentation functions [113]:

$$d\sigma_{UU} = \frac{\alpha^2}{xyQ^2}\frac{y^2}{2(1-\epsilon)}(1+\frac{\gamma^2}{2x})(F_{UU} + \epsilon\cos(2\phi_h)F_{UU}^{\cos 2\phi_h}), \tag{2}$$

$$d\sigma_{UT}^{Collins} = \frac{\alpha^2}{xyQ^2}\frac{y^2}{2(1-\epsilon)}(1+\frac{\gamma^2}{2x})|\mathbf{S}_T|\epsilon\sin(\phi_h+\phi_S)F_{UT}^{\sin(\phi_h+\phi_S)}, \tag{3}$$

$$d\sigma_{UT}^{Sivers} = \frac{\alpha^2}{xyQ^2}\frac{y^2}{2(1-\epsilon)}(1+\frac{\gamma^2}{2x})|\mathbf{S}_T|\sin(\phi_h-\phi_S)F_{UT}^{\sin(\phi_h-\phi_S)}, \tag{4}$$

$$d\sigma_{UT}^{Pretzelosity} = \frac{\alpha^2}{xyQ^2}\frac{y^2}{2(1-\epsilon)}(1+\frac{\gamma^2}{2x})|\mathbf{S}_T|\epsilon\sin(3\phi_h-\phi_S)F_{UT}^{\sin(3\phi_h-\phi_S)}. \tag{5}$$

where γ is defined as $\frac{2Mx}{Q}$ and ϵ is defined as $\frac{1-y-\frac{1}{4}\gamma^2y^2}{1-y+\frac{1}{2}y^2+\frac{1}{4}\gamma^2y^2}$. The x is defined as $\frac{Q^2}{2M\nu}$, y is defined as ν/E and ν is $E-E'$, where E' is the energy of the scattered electron.

The azimuthal angles are defined according to the Trento conventions [114] as shown in Fig. 5. The "F" functions in Eq.2-Eq. 5 are defined as:

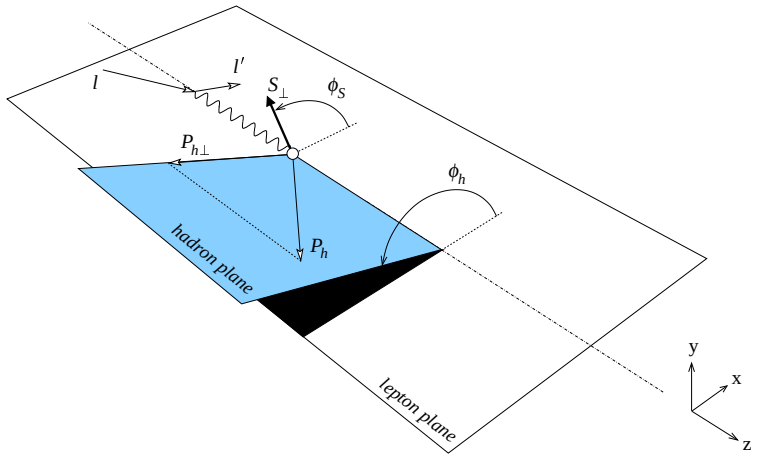

Figure 5: The definition of ϕ_h and ϕ_S according to the Trento conventions.

$$F_{UU} = [f_1 \otimes D_1], \tag{6}$$

$$F_{UU}^{\cos 2\phi_h} = \left[-\frac{2(\hat{\mathbf{h}}\cdot\mathbf{k_T})(\hat{\mathbf{h}}\cdot\mathbf{p_T}) - \mathbf{k_T}\cdot\mathbf{p_T}}{MM_h} h_i^\perp \otimes H_1^\perp \right], \quad (7)$$

$$F_{UT}^{\sin(\phi_h+\phi_S)} = \left[-\frac{\hat{\mathbf{h}}\cdot\mathbf{k_T}}{M_h} h_1 \otimes H_1^\perp \right], \quad (8)$$

$$F_{UT}^{\sin(\phi_h-\phi_S)} = \left[-\frac{\hat{\mathbf{h}}\cdot\mathbf{p_T}}{M} f_{1T}^\perp \otimes D_1 \right], \quad (9)$$

$$F_{UT}^{\sin(3\phi_h-\phi_S)} = \left[\frac{2(\hat{\mathbf{h}}\cdot\mathbf{p_T})(\mathbf{p_T}\cdot\mathbf{k_T}) + \mathbf{p}_T^2(\hat{\mathbf{h}}\cdot\mathbf{k_T}) - 4(\hat{\mathbf{h}}\cdot\mathbf{p_T})^2(\hat{\mathbf{h}}\cdot\mathbf{k_T})}{2M^2M_h} h_{1T}^\perp \otimes H_1^\perp \right] \quad (10)$$

The definition of all TMDs can be found in Fig. 1. D_1 is the unpolarized fragmentation function and $H_1^\perp$ is the Collins fragmentation function. The unit vector $\hat{\mathbf{h}} = \mathbf{P}_{h\perp}/|\mathbf{P}_{h\perp}|$ and the convolution in Eq. 6-Eq. 10 represents an integration over transverse momentum of initial ($\mathbf{p_T}$) and final quark ($\mathbf{k_T}$) with proper weighting [113], i.e.

$$[.. \otimes ..] = x \sum_q e_q^2 \int d^2\mathbf{p_T} d^2\mathbf{k_T} \delta^{(2)}(\mathbf{p_T} - \frac{\mathbf{P_{h\perp}}}{z} - \mathbf{k_T})[...]. \quad (11)$$

These convolutions can be reduced to simple products if the $|P_{h\perp}|$-weighted integrations covers an infinite $|P_{h\perp}|$ or explicit $\mathbf{p_T}$ and $\mathbf{k_T}$ dependencies (like Gaussian distributions) are introduced.

3.2 Transverse target single-spin asymmetry

The target SSA is defined as:

$$A_{UT} \equiv \frac{1}{|S_T|} \frac{d\sigma_{UT}}{d\sigma_{UU}} \quad (12)$$

The Collins, Sivers and Pretzelosity asymmetries have different angular dependence [2]:

$$A_{UT}(\phi_h, \phi_S) \equiv \frac{1}{|S_T|} \frac{d\sigma(\phi_h,\phi_S) - d\sigma(\phi_h,\phi_S+\pi)}{d\sigma(\phi_h,\phi_S) + d\sigma(\phi_h,\phi_S+\pi)}, \quad (13)$$

$$= A_{UT}^{Collins} \sin(\phi_h+\phi_S) + A_{UT}^{Sivers} \sin(\phi_h-\phi_S) \quad (14)$$

$$+ A_{UT}^{Pretzelosity} \sin(3\phi_h-\phi_S). \quad (15)$$

The HERMES [67] and the COMPASS [68] papers used the notation:

$$A_{UT}^{Collins} \equiv 2\langle \sin(\phi_h+\phi_S)\rangle_{UT} \cdot D_{nn} \quad (16)$$

$$A_{UT}^{Sivers} \equiv 2\langle \sin(\phi_h-\phi_S)\rangle_{UT} \quad (17)$$

and

$$\langle \sin(\phi)\rangle = \frac{1}{\pi}\int_0^\pi A_{UT} \sin\phi d\phi \quad (18)$$

[2] In this SSA expression we have not included the Boer-Mulders effect.

where $D_{nn} \equiv (1-y)/(1-y+\frac{y^2}{2})$ for COMPASS. The HERMES definition of D_{nn} includes the longitudinal virtual photon effect $R = \sigma_L/\sigma_T$ and is expressed as $B(y)/A(x,y)$ where $B(y) = (1-y)$, $A(x,y) = \frac{y^2}{2} + (1-y)\frac{1+R(x,y)}{1+Q^2/\nu^2}$. The differences between the HERMES and COMPASS defined D_{nn} are rather small, only at a few percent level.

From Eq. 2-5 we have:

$$A_{UT}^{Collins} \equiv D_{nn} \cdot 2\langle \sin(\phi_h + \phi_S)\rangle_{UT} = D_{nn} \cdot \frac{\left[-\frac{\hat{\mathbf{h}}\cdot\mathbf{k_T}}{M_h} h_1 \otimes H_1^\perp\right]}{[f_1 \otimes D_1]}, \tag{19}$$

$$A_{UT}^{Sivers} \equiv 2\langle \sin(\phi_h - \phi_S)\rangle_{UT} = \frac{\left[-\frac{\hat{\mathbf{h}}\cdot\mathbf{p_T}}{M} f_{1T}^\perp \otimes D_1\right]}{[f_1 \otimes D_1]}. \tag{20}$$

$$\begin{aligned} A_{UT}^{Pretzelosity} &\equiv D_{nn} \cdot 2\langle \sin(3\phi_h - \phi_S)\rangle_{UT} \qquad (21)\\ &= D_{nn} \cdot \frac{[\frac{2(\hat{\mathbf{h}}\cdot\mathbf{p_T})(\mathbf{p_T}\cdot\mathbf{k_T}) + \mathbf{p}_T^2(\hat{\mathbf{h}}\cdot\mathbf{k_T}) - 4(\hat{\mathbf{h}}\cdot\mathbf{p_T})^2(\hat{\mathbf{h}}\cdot\mathbf{k_T})}{2M^2 M_h} h_{1T}^\perp \otimes H_1^\perp]}{[f_1 \otimes D_1]} \end{aligned}$$

Although Eq. 19 and Eq. 20 are defined without any ambiguity, in reality however, different experiments often cover different ranges in the convolution of Eq. 11 due to finite $P_\perp^h$ coverages, making often impossible a direct comparison between A_{UT} results from different experiments. Only after explicit $\mathbf{p_T}$ and $\mathbf{k_T}$ dependencies are introduced, such a comparison becomes meaningful. For an ideal experiment with infinite $P_\perp$ coverage, SSA asymmetries can be weighted by $|P_\perp^h/z_h M_h|$, such that the convolutions in Eq. 11 reduce to products:

$$A_{UT}^{Collins} = \frac{(1-y)}{(1-y+\frac{y^2}{2})} \frac{\sum_q e_q^2 h_1^q(x) \cdot H_1^{\perp(1)q}(z)}{\sum_q e_q^2 f_1^q(x) \cdot D_1^q(z)}, \tag{22}$$

$$A_{UT}^{Sivers} = \frac{\sum_q e_q^2 f_{1T}^{\perp(1)q}(x) \cdot D_1^q(z)}{\sum_q e_q^2 f_1^q(x) \cdot D_1^q(z)}. \tag{23}$$

A slightly different approach, based on an assumed explicit transverse dependence of the TMDs, is followed in Refs. [3, 94, 115].

4 The Proposed Experiment

4.1 Overview

We propose to make precision measurements of the target single spin asymmetry (SSA) in the semi-inclusive deep-inelastic $\vec{p}(e, e'\pi^{\pm})X$ reaction on a 3 cm long upgraded NH_3 target transversely polarized in Hall A with a 100 nA electron beam with energies of 8.8 and 11 GeV. Since the Collins, Sivers, pretzelosity, and other TMD asymmetries are functions of four variables (x, z, P_T and Q^2), precision measurements require both a high luminosity and a large acceptance detection. In the proposed experiment, large coverages of azimuthal angles are important for the separation of different asymmetries which have different azimuthal angular dependence.

The layout of the experiment, as shown in Fig. 6, is the same as that of the approved experiments [108, 112] except using the a polarized proton target instead of a polarized ^{3}He target. The entire detector system consists of two parts: forward-angle detectors and large-angle detectors. The polar angle coverage for the forward-angle detectors is from 9° to 14.3° and the momentum coverage is from 1.0 GeV/c to 7.0 GeV/c. The total solid angle is about 80 msr for this momentum coverage. GEM detectors will be used as tracking detectors (Six layers of the GEM detectors are placed inside the coils. Five of them will be used in tracking for the forward-angle detection). A combination of an electromagnetic calorimeter, gas Cerenkov counters, a layer of Multi-gap Resistive Plate Chamber (MRPC) and a thin layer of scintillator will be used for particle identifications. Although, a 3-bounce Cerenkov geometry is shown in Fig. 6, we plan to use a 1-bounce geometry for the gas Cerenkov. The polar angle coverage for the large-angle detectors is from 17° to 24° which provides additional 160 msr solid angle. They are mainly used for electron detection for a momentum range of 3.5-8.0 GeV/c. The expected π/e ratio is smaller than 1.5. The shashlyk-type calorimeter proposed originally to PAC 35 [108] will be sufficient to provide the pion rejection (200:1). Most recent studies show that a calorimeter based on scintillator fiber (SciFi) technique is also viable. Currently, more detailed studies of performance and cost for both options are ongoing. Four layers of GEM detectors will be used as tracking detectors. The total solid angle is about 240 msr for this momentum range. The acceptance is shown in Fig. 10 and Fig. 11 for electron and pion, respectively.

With the combination of the proposed SoLID, the polarized NH_3 target with its spin which can be polarized both longitudinal and transverse directions and the Jefferson Lab longitudinally polarized electron beam, one can study all leadint twist TMDs discussed in Sec. 1 through SIDIS charged pion and kaon measurements [3]. For SSA asymmetry measurements which are the focus of this proposal, one does not need a polarized electron beam. However, with a polarized electron beam, one can take parasitic measurements of double-spin asymmetry A_{LT} to access g_{1T}.

In this proposal, we focus on measurements of SIDIS charged pions with a transversely polarized NH_3 target to access the proton Collins, Sivers and the Pretzelosity azimuthal asymmetries.

[3] Additional detectors in addition to what have been proposed for SoLID will be needed for kaon detection.

We plan to use the JLab/UVa/SLAC polarized NH_3 target with an upgrade. The polarized NH_3 target has been successfully used in several experiments in Hall C (SANE, RSS and Gen) and at SLAC (E143, E155 and E155x). The target is currently being installed in Hall A for the g2p/GEp experiments, which are scheduled to run from November, 2011 to May 2012. The target is based on the principle of dynamic nuclear polarization (DNP) by using microwave pumping to reach high proton polarizations. The target is operating at a low temperature of 1 K and a strong magnetic field of 5 T. The NH_3 material is chosen because of its proven property of excellent radiation-resistance to electron beam damage to the target polarization. The current achieved best performance for double-polarization experiments with a polarized lepton beam on a polarized proton target was with this target reaching a polarized luminosity of 10^{35} proton/cm^2/s with an in-beam polarization of 80%. Details of the target are described in Sec. 4.2.

A solenoid spectrometer (Solenoidal Large Intensity Device (SoLID)) was proposed for three approved experiments. These include a 11 GeV PVDIS experiment [111], and two SIDIS experiments [108, 109, 112]. Several solenoids with a bore diameter of about 3 m and central field of about 1.5 T have been used in recent experiments (see Table. 4.1). The best magnet option for SIDIS program is the BABAR maget. In this proposal, our study is based on the BABAR solenoid [116], but it will be very similar if we use the Cleo-II magnet, and the kinematic coverage will be reduced by about 20% were the CDF magnet used.

Experiment	B (Tesla)	Bore D (m)	Length (m)	MJ	X_0
BaBar	1.5	2.8	3.46	27	<1.4
Cleo-II	1.5	2.9	3.8	25	2.5
CDF	1.5	2.90	5.00	30	0.85

Table 1: Parameters of recently used solenoidal magnets.

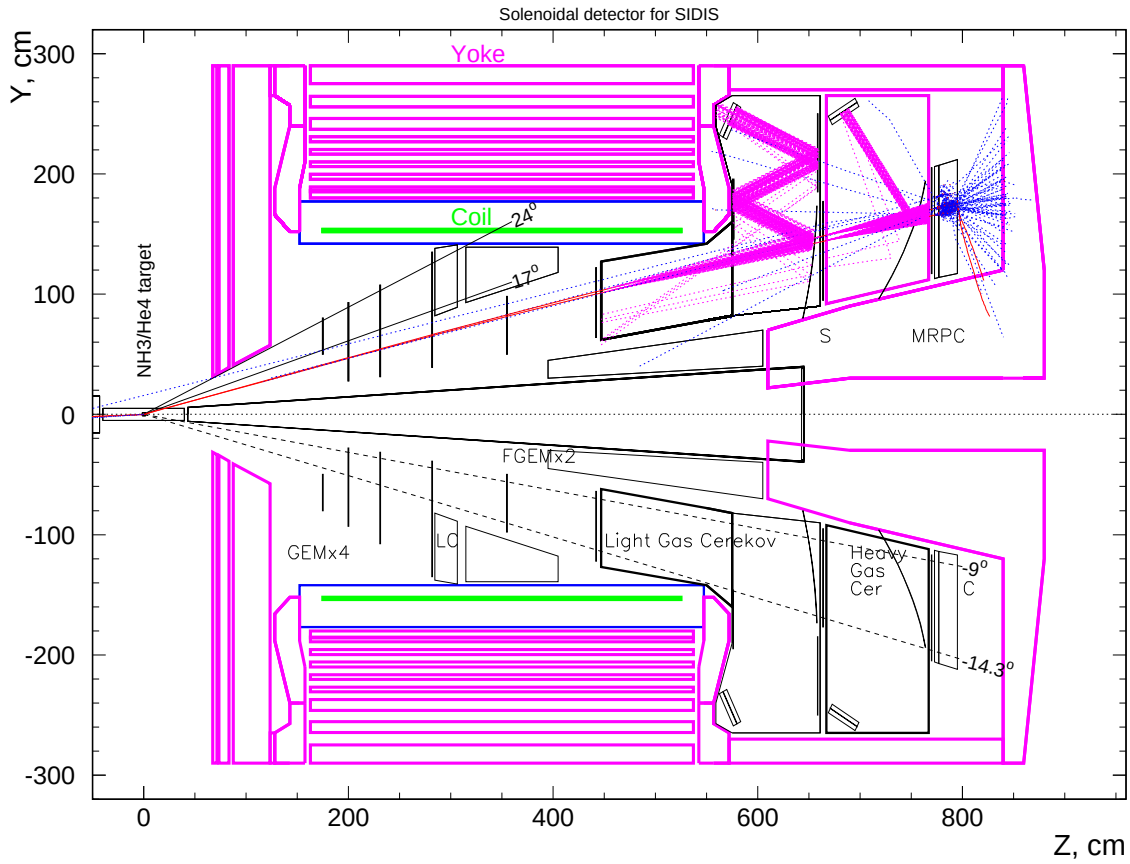

Figure 6: The experimental layout of the SoLID with a polarized NH_3 target. For forward angle detection, there are five layers of GEM detectors ("FGEM") inside the coils in the upstream of the Gas Čerenkov. A 2 m long light Gas Čerenkov is used to separate the electrons and pions. A heavy gas Čerenkov ("HG", 50 cm long) is placed after the light gas Čerenkov to exclude the kaons and the protons from the pions. The shower detector ("S") will be used to provide the trigger, coincidence timing and additional electron/pion separation, especially at high momentum. For the large angle detector, four layers of the GEM detectors ("LGEM") are placed inside the coils. A "shashlyk"-type calorimeter ("LS") will be used to provide trigger, coincidence timing and electron/pion separation.

4.2 Polarized NH_3 target

We propose to us an upgraded version of the JLab/UVa/SLAC polarized NH3 target. The main upgrade will be to use a new magnet to replace the aging Helmholtz-coil magnet and to have fast spin-flip capability with the AFP technique. The target is based on the principle of dynamic nuclear polarization (DNP) by using microwave pumping to reach high proton polarizations [117, 118].

The target is operating at a low temperature of 1 K and a strong magnetic field of 5 T. The NH3 material is chosen because of its proven property of excellent radiation-resistance to electron beam damage to the target polarization. The current achieved best performance for such kind of experiments with a polarized lepton-beam on a polarized proton target was with this target which reached a luminosity of 10^{35} proton/cm^2/s with an in-beam average polarization of 80%. In this experiment, the ability to flip the target polarization frequently is important for the proposed SSA measurements in terms of reducing systematics. Adiabatic fast passage (AFP) NMR has been demonstrated as an effective (90% efficiency) way of spin flip for a DNP target with ^{7}LiH as a target material [119], no AFP spin flip test has been reported for NH_3 in the literature. The most current information on the efficiency of AFP spin-flip for NH3 is in a proceeding from a recent workshop [120] in which it was expected to be about 50% for the condition at 5T/1K. This proposal will use this number as the base for calculating the average polarization with spin flip. While AFT spin flip R&D tests [121] for NH_3 are being planned for the near future, ^{7}LiH is another possible target material with even a better dilution factor (~ 0.25) than that of NH_3 (~ 0.18) for this experiment, while the main drawback would be the slow spin-up time.

A set of superconducting Helmholtz coils provide a 5-T field with a highly uniform area, about 3 cm $\times$ 3 cm $\times$ 3 cm in the center. The existing magnet was designed mainly for longitudinal polarization while also allowing transverse polarization. In the longitudinal case, it has a large opening in the forward region ($\pm 45^\circ$) for scattered particles to be able to reach the spectrometer/detector system, while in the transverse case, it has only about $\pm 17^\circ$ nominal opening in the forward region. The new design will optimize to allow both transverse and longitudinal to have a nominal forward opening of more than $\pm 28^\circ$, while maintain the same maximum field and uniform field region in the center.

A couple of target cells with length of 3 cm are immersed in a vessel filled with liquid helium which was maintained at 1 K by a series of large pumping system. The target cell is filled with beads of solid NH3 material with a typical packing factor of about 50% with the rest of the space filled with helium. It may be possible to increase the packing fraction to $70 - 80\%$ by changing NH_3 beads to disks. The R&D efforts related to this issue are being planned by the JLab polarized target group. The target material is usually prepared by irradiation before-hand at a low energy electron facility, such as NIST. During the experiment, the target material is exposed to 140 GHz microwaves to drive the hyperfine transition which aligns the proton spins. The DNP technique produces proton polarizations of greater than 90% in the NH3 target. The heating of the target by the beam causes a drop of a few percent in the polarization, and the polarization slowly decreases with time due to radiation damage. Most of the radiation damage can be repaired by annealing the target at about 80 K, until the accumulated dose reached

is greater than about 17×10^{15} e^-/cm^2, at which time the target material needs to be replaced.

Target polarization is measured with an NMR system, which is calibrated with a measurement of polarization in thermal equilibrium (TE). Typical precision reached in the polarization measurement is about 3%.

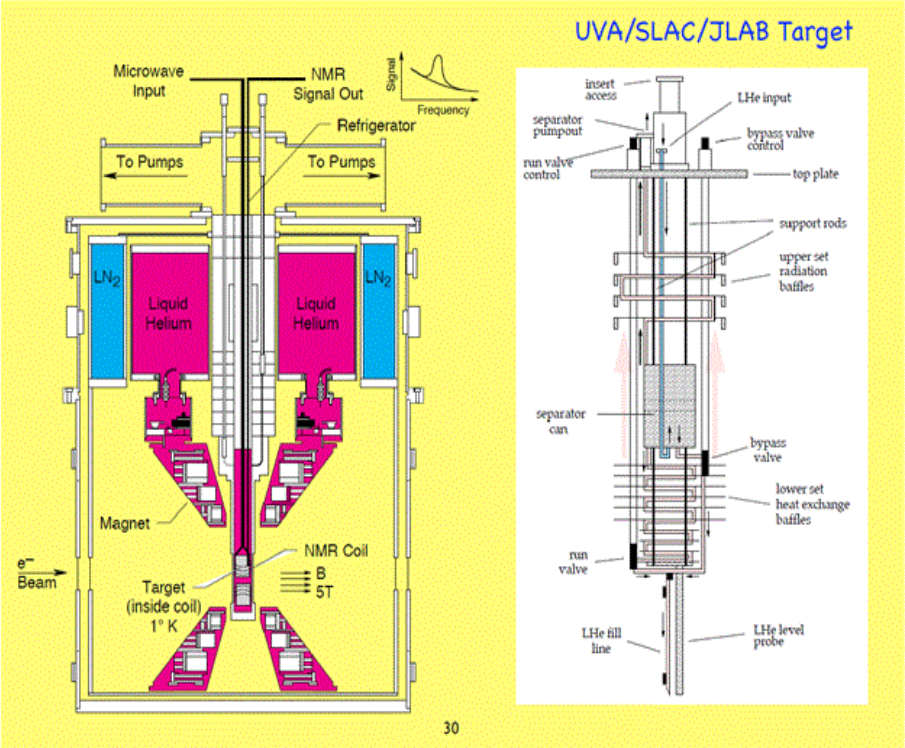

Figure 7: Polarized target system

For transverse polarization, the target field is perpendicular to the beam axis. This creates a deflection of electron beam (which is more significant for lower beam energies). To ensure proper transport of the beam, a chicane will be employed. A beam chicane system has been developed for the g2p/GEp experiments which will be more than enough to satisfy the need of this proposed experiment. Th electron beam will be pre-bended such that the outgoing beam after the target will be going straight to the regular Hall Abeam dump. No local beam dump will be necessary as in the g2p/GEp case.

To reduce the target depolarization due to beam, a large size (2.5 cm) raster system (slow-raster) will be used in addition to the existing Hall A fast-raster system. The typical beam current this target can tolerate is about 100 nA. Beam diagnostic system (beam current and position measurement system) which can handle such a low current will be needed.

Fortunately, all of the above beam-line system has been developed and is being implemented for the upcoming g2p/GEp experiments. The beam diagnostic system is compatible with the high beam energies. Minor modifications will be needed to make the slow raster working with high beam energies.

4.3 Acceptance and Kinematic Coverage

With the target field, the polar angle coverage for electrons θ_e is from 3° to 28°. Although the current UVA/JLab polarized NH_3 target has about $\pm 16^0$ forward opening in the transverse spin configuration, the planned upgrade will have a new magnet designed to have optimized geometry for transverse polarization such that it will have forward opening of more than ±28°. The acceptance study assumed the upgraded configuration with no forward angle limitation.

The effect on the azimuthal angular coverage from the polarized NH_3 target field is significant, and has been studied by GEANT3 Monte Carlo simulation which includes realistic spectrometer models, detector geometries, and the target field [4]. A very important experimental issue associated with such a target in a strong transverse field, known as "line of flame" is clearly shown in our simulations, where extremely high backgrounds are seen in highly localized areas of the acceptance. As an example, Fig. 8 shows the radius vs. azimuthal angular coverage in lab frame on GEM chamber 1. One way to get around this issue is to "remove" certain areas of the detectors where "line of flame" passes through as shown in 9 by turning off part of the detectors. The other way is to add collimators in the target region to block these high rate regions more efficiently. The corresponding acceptance for electron (charged pion detection) is shown in Fig. 10 (Fig. 11). While the simulation results show that the θ angular distribution of acceptance extends to both smaller and larger angles, the acceptance of ϕ at forward angle decreases by 30 % and at large angle by 20%. Based on our previous GEANT3 studies for SoLID experiment PR12-10-014 and E12-10-006, resolutions are not issues for the proposed SIDIS experiment. Reconstruction of angles is more important which can be addressed by careful simulations of the optics before the experiment and calibration during the experiment. Optics studies based on Monte Carlo simulations have been completed recently for the g2p/GEp experiment employing also the transversely polarized NH_3 target in Hall-A, and a careful optics study with beam is being planned for the these experiments. Our proposed experiment will benefit from the experience of the upcoming g2p/GEp experiments which are scheduled to run in the fall of 2011.

The kinematic coverages are shown in Fig. 12 (Fig. 13) for 11 GeV (8.8 GeV) with cuts for $Q^2 \geq 1$ $(GeV/c)^2$ (DIS), W $\geq$ 2.3 GeV, W' $\geq$ 1.6 GeV (avoid resonance region) and $0.3 < z < 0.7$ (current fragmentation and factorization). The two-dimensional azimuthal angular coverage for both forward and large angle regions for Collins, Sivers, and pretzelosity asymmetry measurements at 11 GeV (8 GeV) are shown in Fig. 14 (Fig. 17), and Fig. 15 (Fig. 17), respectively. The final kinematic coverage is x = 0.05 - 0.68, Q^2 = 1.0 - 9.0 $(GeV/c)^2$. The resulting transverse momentum of the hadron, p_T coverage is between 0 and 1.8 GeV/c for the 11 GeV incident beam with the target field. We organize the kinematic binnings as following: Q^2 coverage (from 1 to 9 $(GeV/c)^2$) is divided into 8 bins; transverse momentum P_T coverage (from 0 to 1.8 GeV/c) is divided into 9 bins; z coverage of 0.3 to 0.7 is divided into 8 bins, and the x coverage from 0.05 to 0.68 is divided according to the projected statistics within the bin. In the projection, the total number of bins is more than 650, and these results will allow for a map of the Single target Spin

[4] The exisiting SLAC/UVA/JLab NH_3 target field map is used in the GEANT3 simulations, though a new magnet optimized for the proposed experiment will be needed.

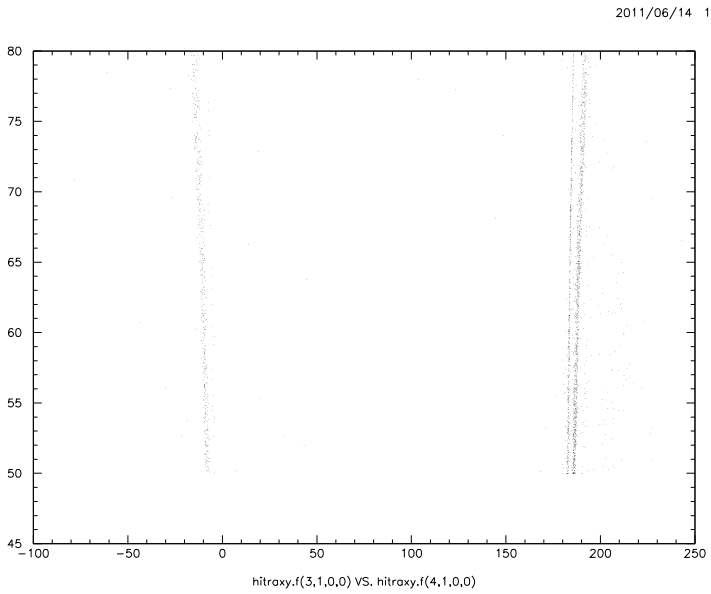

Figure 8: GEANT3 simulation results of "line of flame" with NH_3 target field on. The x-axis is the azimuthal angle in lab frame. The y-axis is the radius of GEM chamber 1. Two lines of flame are clearly shown in two narrow range of azimuthal angle ϕ.

Asymmetries in four dimensions (x, Q^2, z and p_T).

4.4 Estimation of Rates

For the SIDIS $(e, e'\pi^{\pm})$ reaction, we have assumed a beam current of 100 nA, a target length of 3 cm mixture of NH_3 and ^{4}He and an average in-beam target polarization of 70% (with a spin flip every 60 minutes). The overall detection efficiency is assumed to be 70% which includes the detection efficiency, computer dead time and electronic dead time. Singles rates from various processes have also been calculated using a realistic detector and target geometry in the GEANT3 simulation. The regions corresponding to "lines of flame" (shown in Fig. 9) are also removed for this calculation. The singles rates were estimated using Whitlow/QFS and Wiser codes. These codes have been previously checked and matched with the Hall-A E06-010 data. Table 2 shows the coincidence rates and singles rates for electrons and pions. For the forward detection the low momentum cut-off is about 1.0 GeV/c and for the large angle detection the cut-off is about 3.5 GeV/c. In general, the estimated rates are lower by a factor of 5-10 than those of ^3He proposal [108, 112]. Such a difference in rates are consistent with the difference in unpolarized luminosities. Similarly, the high energy photon background from π^o decay is also not an issue based on the same argument of luminosity difference.

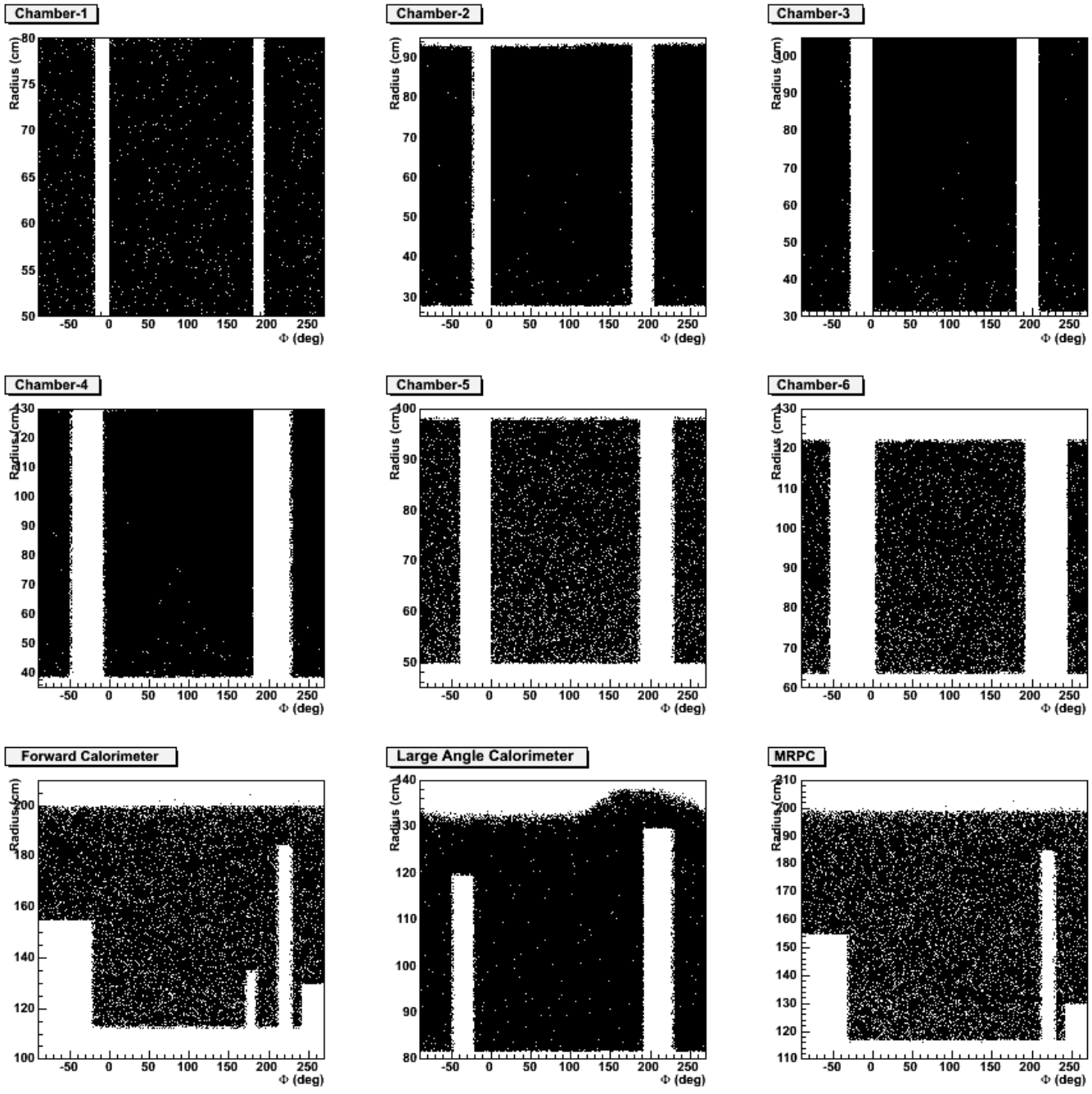

Figure 9: Cuts shown in detector acceptance to remove "line of flame". The top six panels show the acceptance on GEM chambers. The 7th and 8th panel shows the acceptance on forward and large angle calorimeters. The last panel shows the acceptance of MRPC.

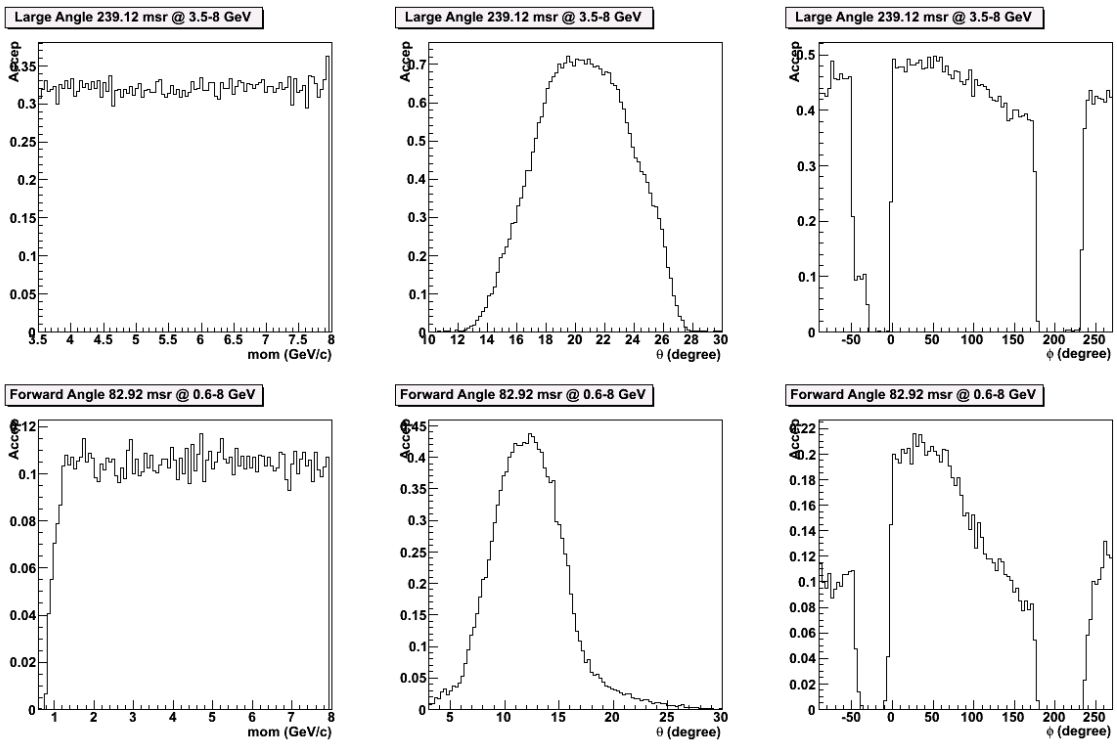

Figure 10: GEANT3 simulation results of electron acceptance with NH_3 target field on with certain area removed to avoid "line of flame". Top and bottom panels show the acceptance of large and forward angle detection, respectively. The total solid angle in the accepted momentum range are also listed.

Process	Forward angle 11 GeV	Large angle 11 GeV	Forward angle 8.8 GeV	Large angle 8.8 GeV
(e,eπ^+)	187 Hz	11.6 Hz	161 Hz	7.3 Hz
(e,eπ^-)	243 Hz	14.6 Hz	235 Hz	10.5 Hz
single e^-	22.2 kHz	0.65 kHz	34.5 kHz	0.87 kHz
single π^-	299 kHz	0.65 kHz	260 kHz	0.39 kHz
single π^+	520 kHz	2.73 kHz	455 kHz	1.65 kHz

Table 2: Singles rates for different particles with 11 GeV and 8.8 GeV beam.

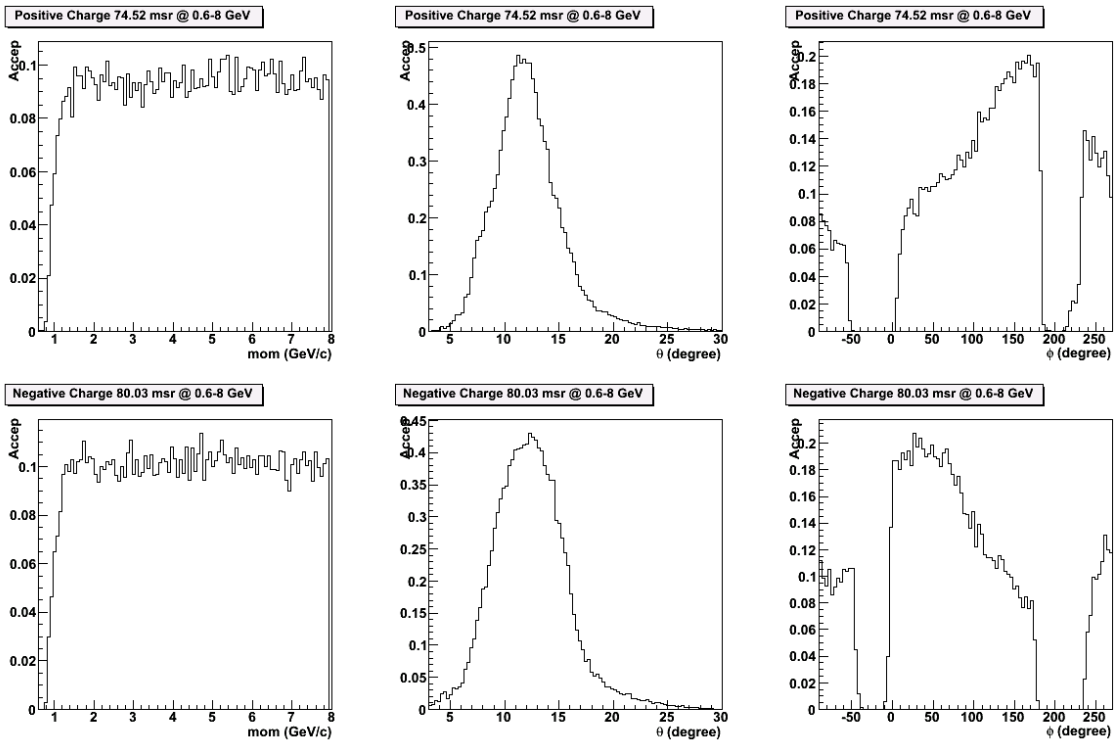

Figure 11: GEANT3 simulation results of charged pion acceptance with NH_3 target field on at forward angle with certain area removed to avoid "line of flame". Top and bottom panels show the acceptance for positive and negative charged pions, respectively. The total solid angle in the accepted momentum range are also listed.

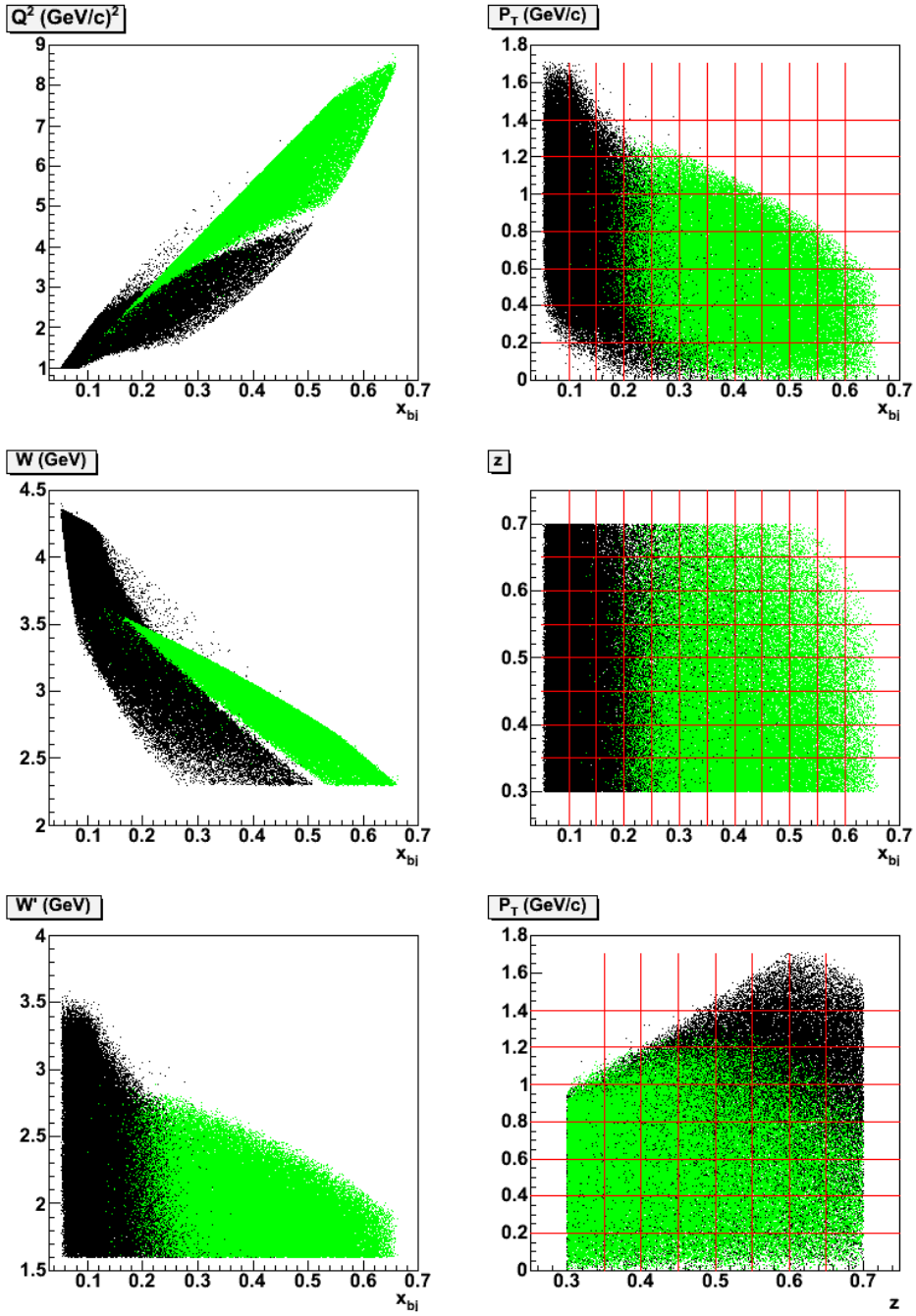

Figure 12: SIDIS kinematic coverage for an 11 GeV electron beam with polarized NH_3 target field on. The coverage for the forward-angle (large-angle) detectors are shown as black (green) points.

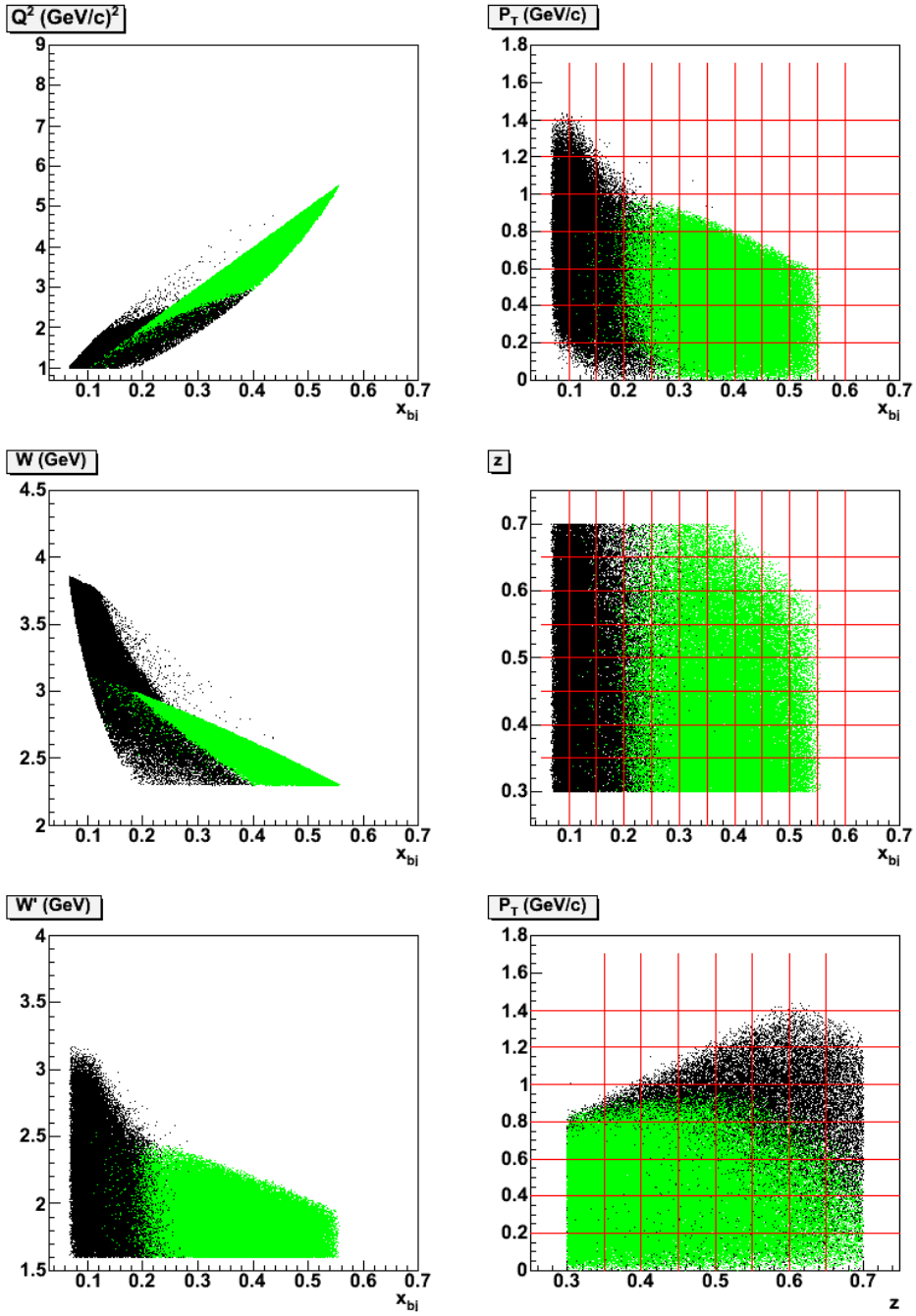

Figure 13: SIDIS kinematic coverage for an 8.8 GeV electron beam with polarized NH_3 target field on. The coverage for the forward-angle (large-angle) detectors are shown as black (green) points.

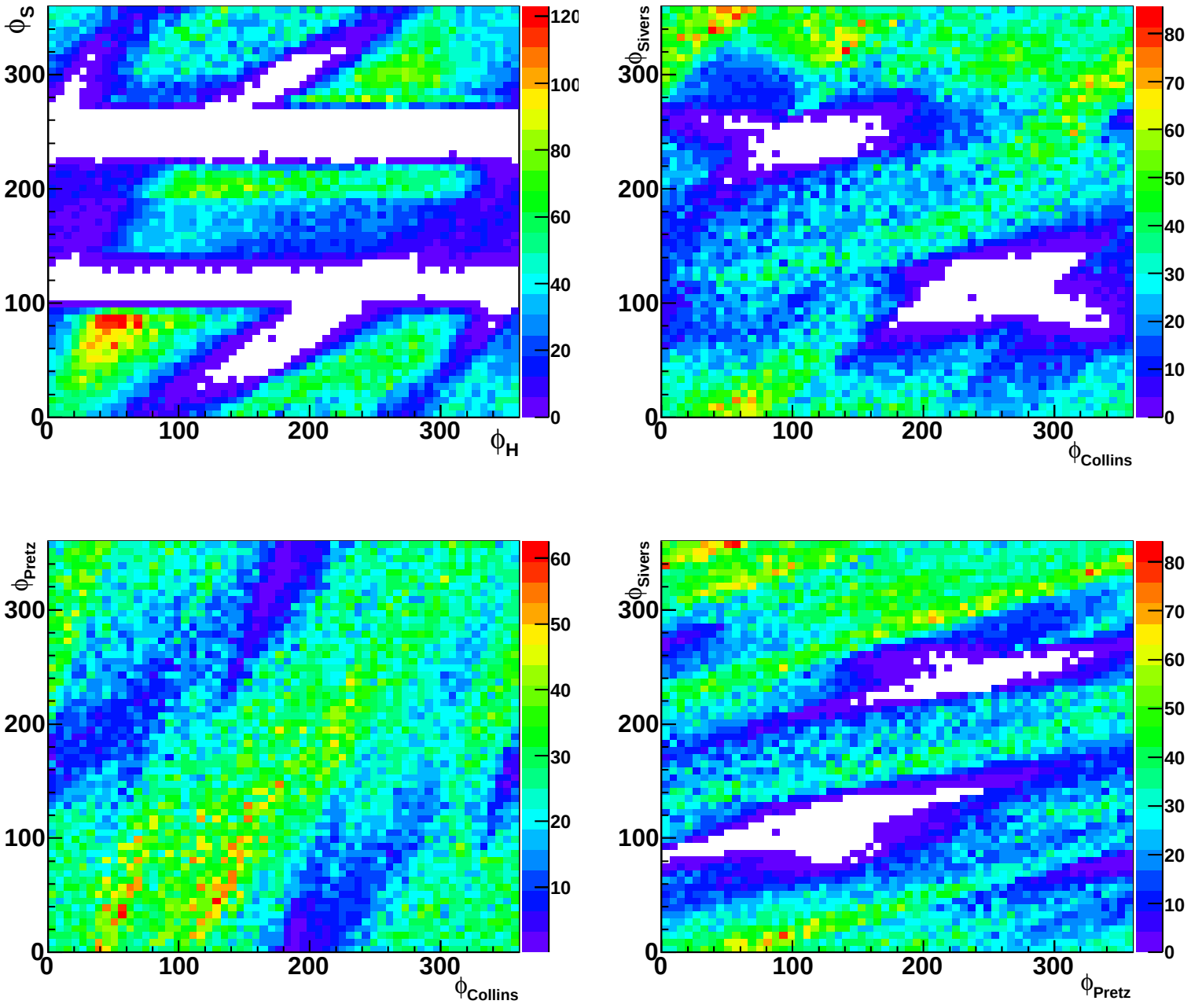

Figure 14: Two-dimensional azimuthal angular coverage for Collins, Sivers and pretzelosity asymmetry measurements in the forward angle region for an 11 GeV electron beam with a transversely polarized NH_3 target.

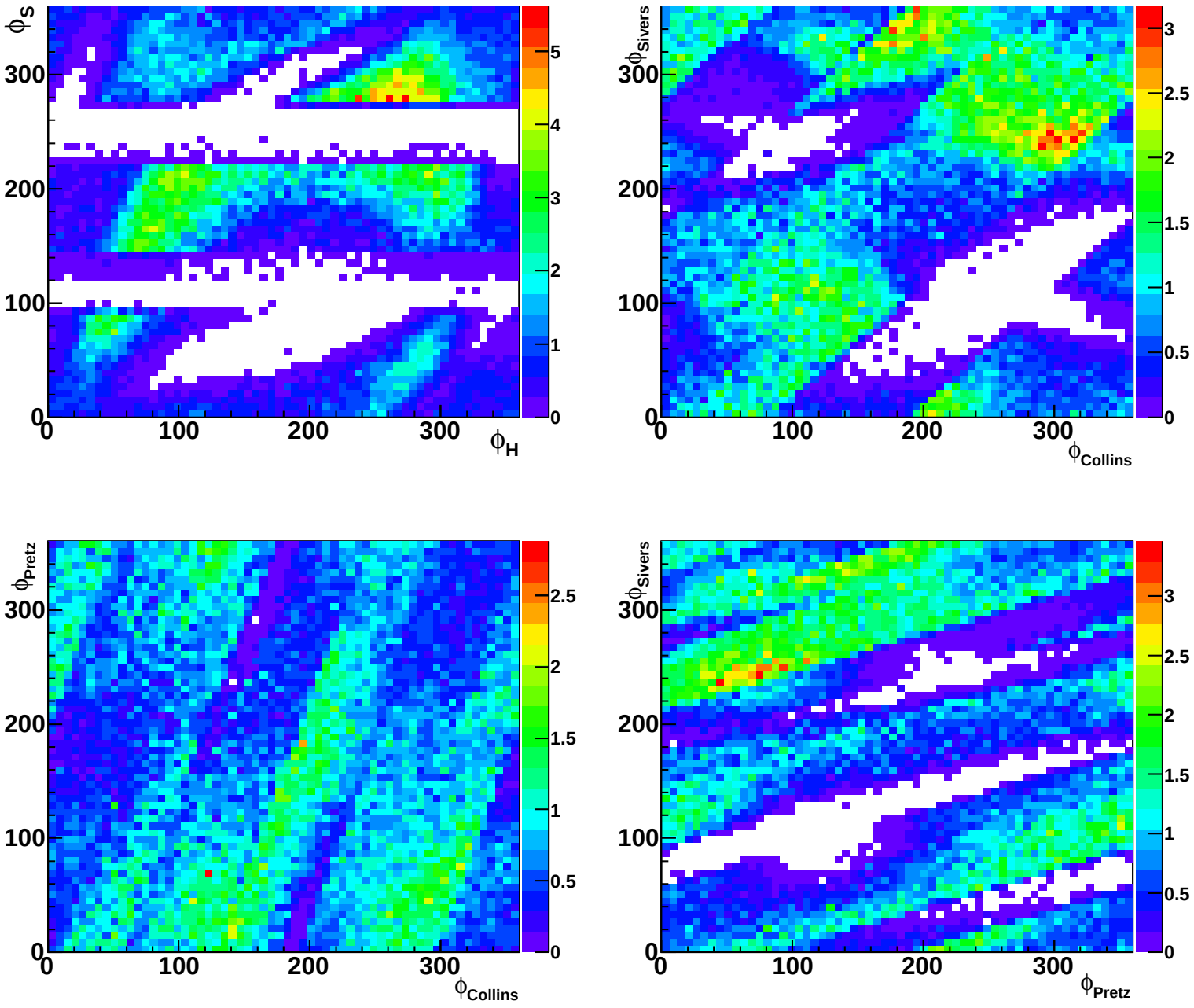

Figure 15: Two-dimensional azimuthal angular coverage for Collins, Sivers, and pretzelosity asymmetry measurements in the large angle region for an 11 GeV electron beam with a transversely polarized NH_3 target.

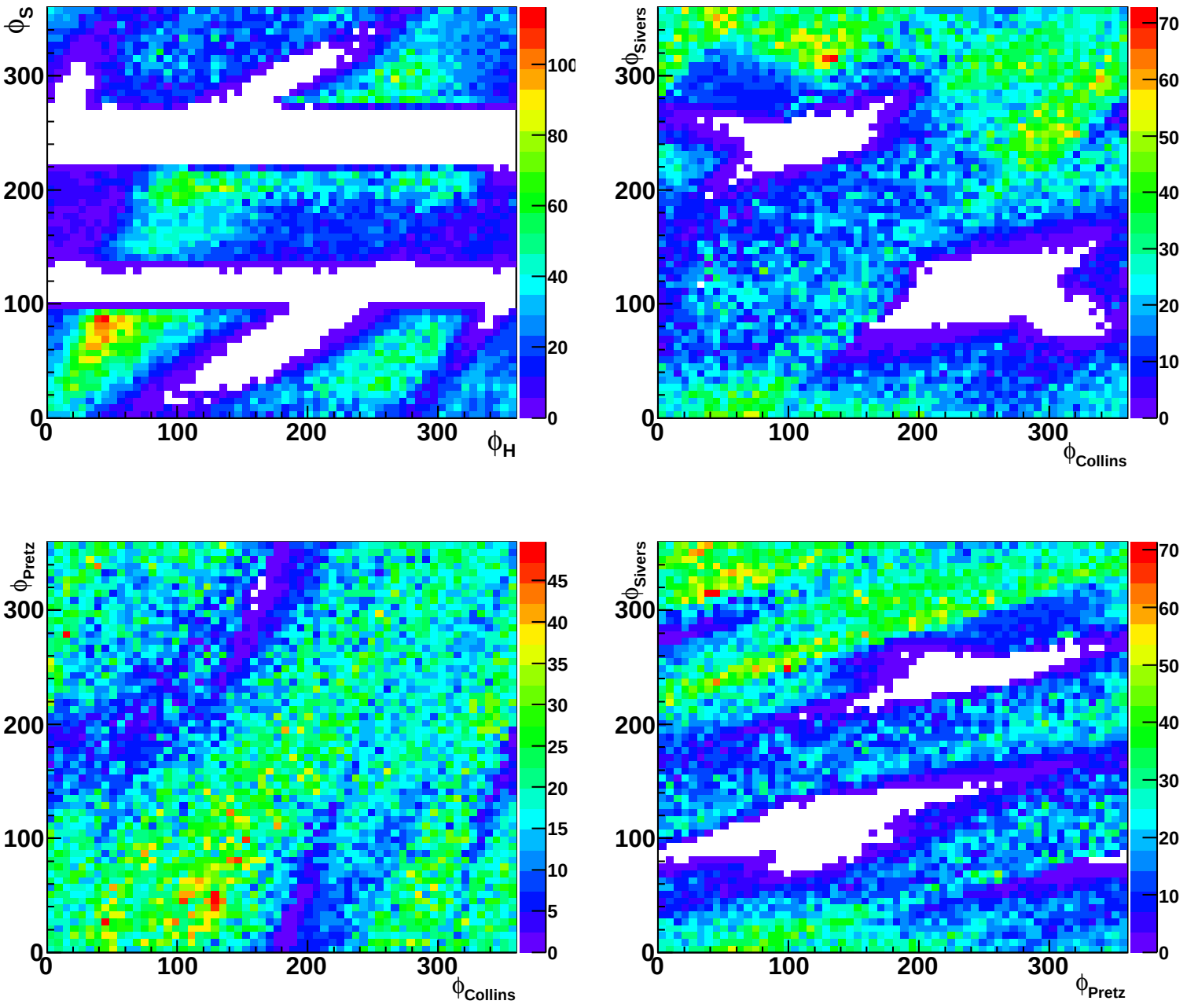

Figure 16: Two-dimensional azimuthal angular coverage for Collins, Sivers, and pretzelosity asymmetry measurements in the forward angle region for an 8.8 GeV electron beam with a transversely polarized NH_3 target.

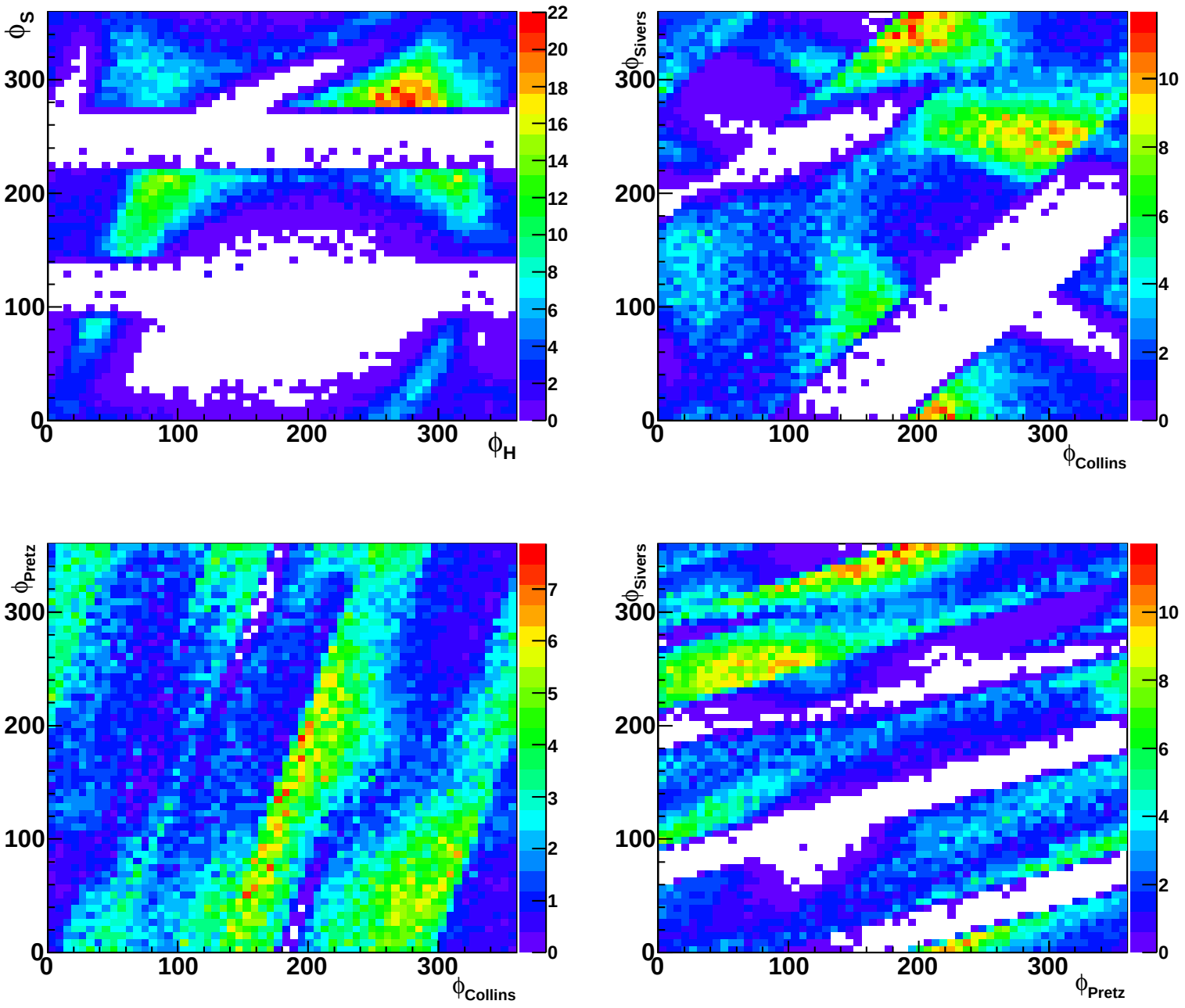

Figure 17: Two-dimensional azimuthal angular coverage for Collins, Sivers, and pretzelosity asymmetry measurements in the large angle region for an 8.8 GeV electron beam with a transversely polarized NH_3 target.

4.5 Detectors

In this experiment, we propose to use the same setup as in the approved ^{3}He SoLID SIDIS proposals [108, 109, 112] with cerntain regions of detectors disabled (or removed) for the "line of flames". In this section, we will focus on the new dedicated studies on the current setup.

4.5.1 GEM Trackers and Background Rates

A total of six GEM trackers will be used to provide the momentum, angle and interaction vertex of the detected particle. For the forward-angle detection, except for the first layer, all other layers will be used. For the large-angle detection, the first four layers of GEMs will be used, where the background rate is expected to be smaller than the forward-angle. The detector configuration is shown in Fig. 6.

The background rates on the GEM detectors were estimated using GEANT3 simulation with all the physics processes(such as Moller/Mott etc) turned on. The background simulation after removing the "line of flame" shows that the rates on the GEM chambers similar to those estimated for the ^{3}He proposal. Fig. 18 shows the results obtained from the simulation for two different beam energies (11 GeV and 8.8 GeV). The estimated background rates are much smaller than 30 KHz/mm^2, in which GEMs have been used in the COMPASS experiment. At the proposed background rates, tracking has been sucessfully demonstrated with the proposed configuration in ^{3}He proposal [108, 109, 110, 112].

4.5.2 Expected Resolutions

The optics of the BaBar magnet is studied which includes the target field of the current UVA/JLab polarized proton target. Fig 19 shows the resolutions obtained from the simulation for different polar angles (θ), and shown as a function of momentum of the scattered particle. The interaction vertex position resolution is assumed to be 1.5 cm, which is determined by the target length. A 200 μm position resolution on GEM is assumed. The resulting momentum resolution $\frac{\delta p}{p}$ is about 1% (σ), with a larger resolution at high momentum. For angular resolution, instead of using the common polar angle θ and azimuthal angle ϕ in the lab frame, we decided to use $\frac{dx}{dz}$ and $\frac{dy}{dz}$. Here, $\frac{dx}{dz}$ is the slope of tracks in the plane perpendicular to the target holding field. $\frac{dy}{dz}$ is the slope of the tracks in the plane of the target holding field and the incident beam direction. The average $\frac{dx}{dz}$ and $\frac{dy}{dz}$ are about 0.007 and 0.0012, respectively. The main reason that the resolution on $\frac{dx}{dz}$ is much larger than $\frac{dy}{dz}$ is due to the extended target length.

Fig. 20 shows the resolutions of the kinematic variables x, Q^2, z, P_T, ϕ_s and ϕ_h, after including the resolution on momenta of the scatterted electron and the leading hadron and slopes of directions of incident electron, scattered electron and the leading hadron. The resolution in x, Q^2, z, and P_T are much smaller than the proposed bin size. Furthermore, the maximum resolution in ϕ_s and ϕ_h are 1.14° (small x) and 5.7° (small P_T), respectively. The systematic uncertainties on Collins and Sivers effect are below 0.5% (relative), assuming a resolution of 1.14° and 5.7° of ϕ_s and ϕ_h. The effect on pretzlosity is below 2.5% (relative) in comparison.

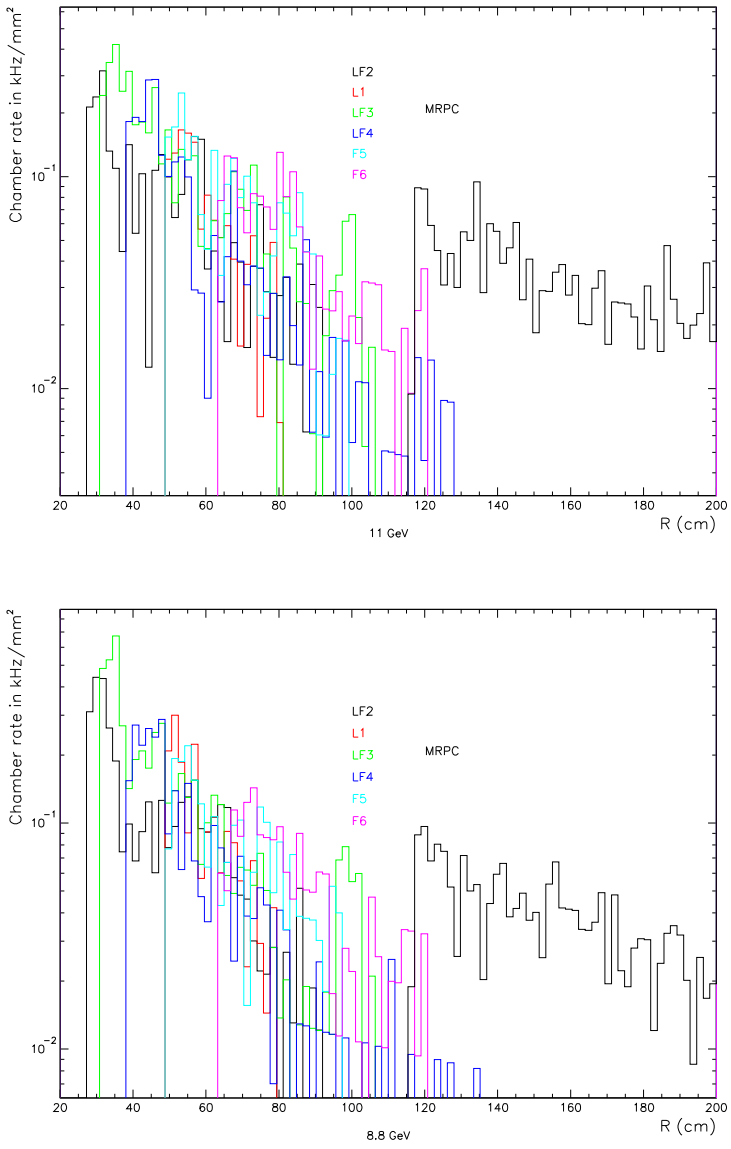

Figure 18: The simulated background for 11 (8.8) GeV beam is shown in upper (lower) panel. The rate on each GEM layer is plotted as a function of its radius. The label "L1" denotes the first layer in the large-angle. "LF2", "LF3" and "LF4" are shared between the large-angle and forward-angle detection. The "LF5" and "F6" are used in the forward-angle only.

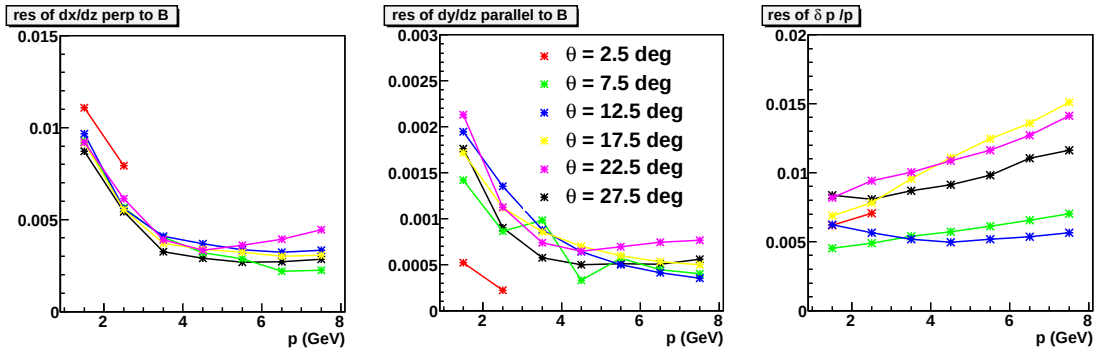

Figure 19: The resolutions of dx/dz, dy/dz and momentum. The x axis is the momentum of the particle.

4.5.3 Electromagnetic Calorimeter

A "shashlyk" type electromagnetic calorimeter will be used in both forward and larger angle to identify electrons and hadrons. The calorimeter will be split into preshower/shower type configuration, which can give a pion rejection factor of 100:1 with E > 1.0 GeV and an energy resolution of $\leq 5\%/\sqrt{E}$.

The Shashlyk type calorimeter is a sampling type calorimeter constructed from alternating layers of scintillator and heavy absorber. The scintillation light is carried to the photon detector by a wave-length shifting optical fibers running longitudinally through the calorimeter. The calorimeter design is currently being studied using a GEANT4 simulation. An optimal design is considered to reach the required goals on the pion-rejection and energy resolution. In a typical design, each layer consists of 1.5 mm thick scintillator plate and a 0.6 mm thick absorber. The effective radiation length (X_0) is about 21 mm. More details on the status of the calorimeter design can be found in the updated proposal E12-11-007 to PAC38 [112].

The background rates on the calorimeter have been calculated using the GEANT3 simulation for this experiment, and the results are shown in Fig. 21. With further optimization of the setup we can reduce the background rates on the calorimeter. Overall the background level is at most comparable to that of the approved experiments using the ^{3}He target [108, 112].

4.5.4 Particle Identification Detectors

For electron detection, a light gas Cerenkov will be used to combine the electromagnetic calorimeter system at forward angle. An E&M calorimeter will be enough to provide electron PID at large angle, where the pion/e ratio is expected to be smaller than 1.5 for particles with momentum larger than 3.5 GeV. The pion PID will be provided by a MRPC time-of-flight detector (separate from protons, and kaons at low momentum), gas Cerenkov and E&M calorimeter (separate from electrons), and a heavy gas Cerenkov (separate from kaons at high momentum). The background rate of MRPC is also simulated through GEANT3 program and shown in Fig. 18. The baseline parameters of detectors are assumed to be same as in Ref. [108, 112]. A beam test of a prototype MRPC for

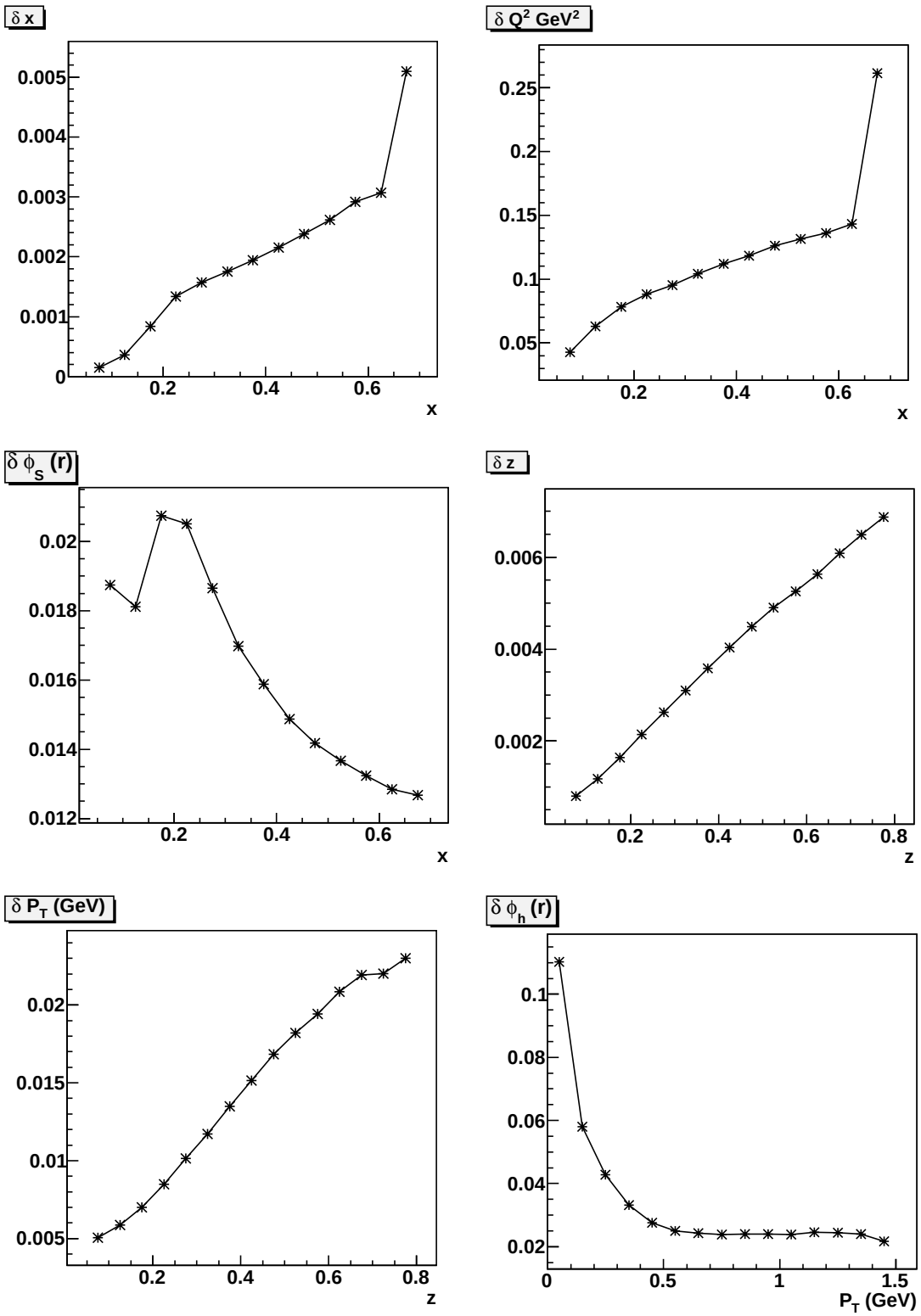

Figure 20: The resolutions of kinematic variables x, Q^2, ϕ_s, z, P_T, ϕ_h.

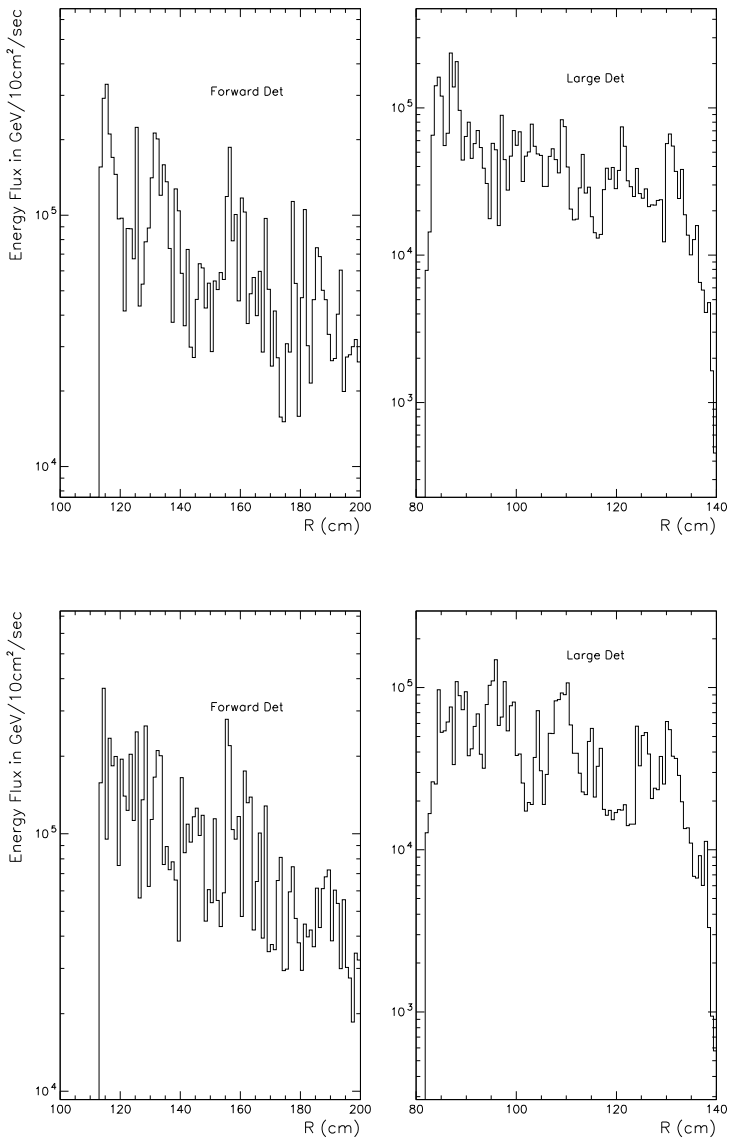

Figure 21: The energy flux (in GeV/10cm^2/sec) on the calorimeter as a function of its radius. The left (right) panel shows the background for the forward-angle (large-angle) detector.

SoLID in Hall A is planned for fall 2011.

4.5.5 Update on Cerenkov Detectors

This experiment requires both electron and pion detection. In order to unambiguously identify both electrons and pions several PID detectors will be required. Two Cherenkov detectors will be an essential part of the PID scheme.

Electron identification: the light-gas Cherenkov

A Cherenkov detector filled with CO_2 at 1 atm would ensure electron-pion separation up to a momentum of 4.65 GeV. This detector, extending 2.1 m along the beam line, would be positioned immediately after the SoLID coil. The close proximity to the SoLID magnet requires careful consideration of various options for the photon detectors. In addition, the detector optical system is expected to provide full coverage in the azimuthal angle.

Recently a GEANT4 simulation was used to optimize the design of the optical system. It was found that with just one system of 30 spherical mirrors (following the SoLID sectoring) near perfect collection efficiency, $> 95\%$, can be achieved with a $12''$ by $12''$ photon detector (active area). This size could be easily scaled down to $6''$ by $6''$ by employing Winston cones. A schematic of this setup is shown in Fig. 1 where Cherenkov photons (green) produced by the passage of electrons (red) through the radiator gas are reflected by 30 spherical mirrors (grey) and focused onto the photon detectors (cyan).

The one-mirror optical system is a significant improvement over the three-mirror design outlined in the proposal presented to PAC35. The Cherenkov photon yield lost due to reflections off multiple mirrors is reduced. This is particularly important for the GEM + CsI option where is technically challenging to manufacture and maintain mirrors with good reflectivity in the UV region. In addition the one-mirror design is more practical and cost efficient form the manufacturing and installation point of view.

The same GEANT4 simulation has been used to describe the photon detector response and this is yet another improvement since PAC35. Two options have been considered for the photon detectors: magnetic field resistant photomultiplier tubes, PMTs, (Fig. 1, left panel) to be used in combination with Winston cones and gaseous electron multipliers with Cesium Iodide coating, GEMs + CsI, (Fig. 1, right panel).

For the PMT option the Hamamatsu model H10966A-100 was considered. This is a $2''$ multi-anode PMT with up to 94% photocathode coverage and good quantum efficiency down to wavelengths of 200 nm. These characteristics make this model ideal for tiling and we plan to use 9 such PMTs per sector, in a 3 by 3 array, to cover a $6''$ by $6''$ area. It is fairly resistant in magnetic field: such unshielded PMT experiences up to 60% gain reduction in 100 Guass field according to data provided by Hamamatsu. This is a significant improvement when compared to a regular $5''$ PMT which,if unshielded, would experience a similar gain reduction at only 4 Gauss. To establish whether H10966A-100 could withstand the magnetic field of SoLID we plan to test it with shielding this Summer at Temple University. If the magnetic field test results are satisfactory we plan additional tests at Jefferson Lab to ensure suitability in high-background environment.

An estimate of the number of photoelectrons for this option with the configuration described above (Fig. 1, left panel) yields between 25 and 35 photoelectrons. The number

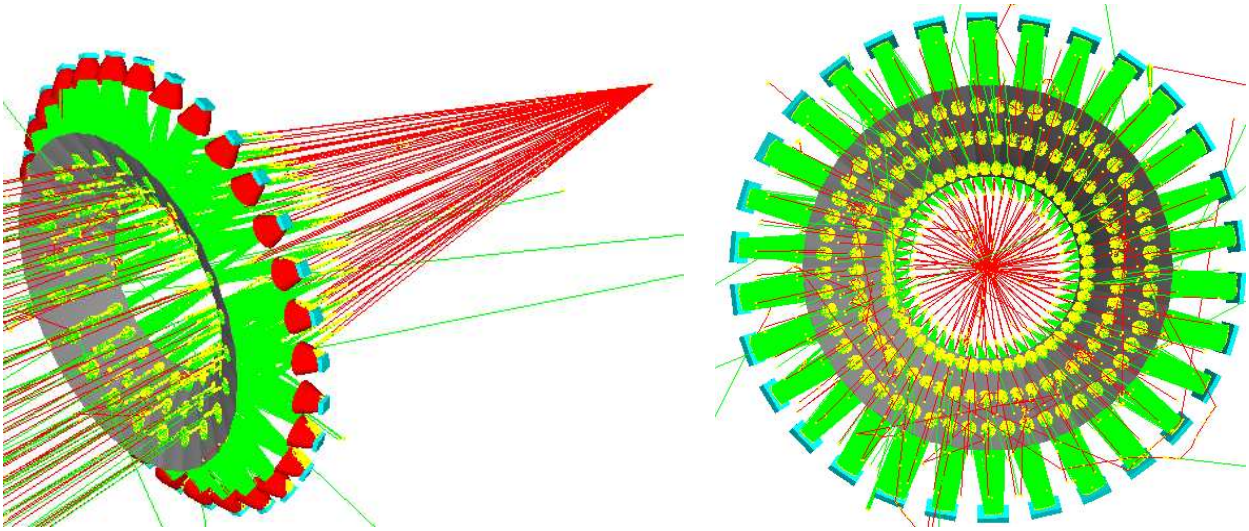

Figure 22: Setup of the light-gas Cherenkov: a system of 30 spherical mirrors (grey) will focus the Cherenkov photons (green) created by the passage of electrons (red) through a radiator gas onto photon detectors (cyan). Left panel: setup for the PMT option, side view (see text). Right panel: setup for the GEM + CsI option, back view - as seen from the beam dump (see text).

depends slightly on the electron polar angle: because of the mirror positioning in the tank electrons with higher polar angles traverse a longer path in the radiator gas than those with lower polar angles. This estimate includes wavelength dependent corrections like mirror and Winston cones reflectivities and the PMTs quantum efficiency as well as an overall correction of 0.8 to account for the reduction in the photocathode effective area as a result of tiling.

The GEM + CsI is an alternative to the PMT option and has the clear advantage of being resistant in magnetic filed. This has been used successfully as a photon detector during PHENIX experiment at BNL in a Hadron Blind Detector [122] and a similar setup is being developed in Japan for use in JPARC experiments [123]. The photon detector consists of three layers of GEMs the first being covered with CsI which acts as a photocathode. The operational regime for CsI is the ultraviolet (UV) region, between 120 and 200 nm [124]. This requires a radiator gas with good transparency in the UV and with very good purity to avoid photon absorption by impurities. Thus for the GEM + CsI option, a suitable gas choice would be CF_4 which, unlike CO_2, is transmissive between 120 nm and 200 nm [125]. This gas would still give an acceptable threshold for electron-pion separation and it was the gas of choice for the successful PHENIX run.

The number of photoelectrons for this option was estimated using the GEANT4 simulation and assuming a $12''$ by $12''$ photon detector (Fig. 1, right panel). A signal of 20 to 30 photoelectrons was obtained. Wavelength dependent corrections as mirror reflectivity and quantum efficiency of CsI were taken into account as well as an overall correction of 0.54 to account for loss of signal due to gas transparency, reduced photocathode coverage of the GEM (about 20% of the GEM surface is occupied by holes), transport efficiency of avalanche electrons through gas, etc.

Pion identification: the heavy-gas Cherenkov

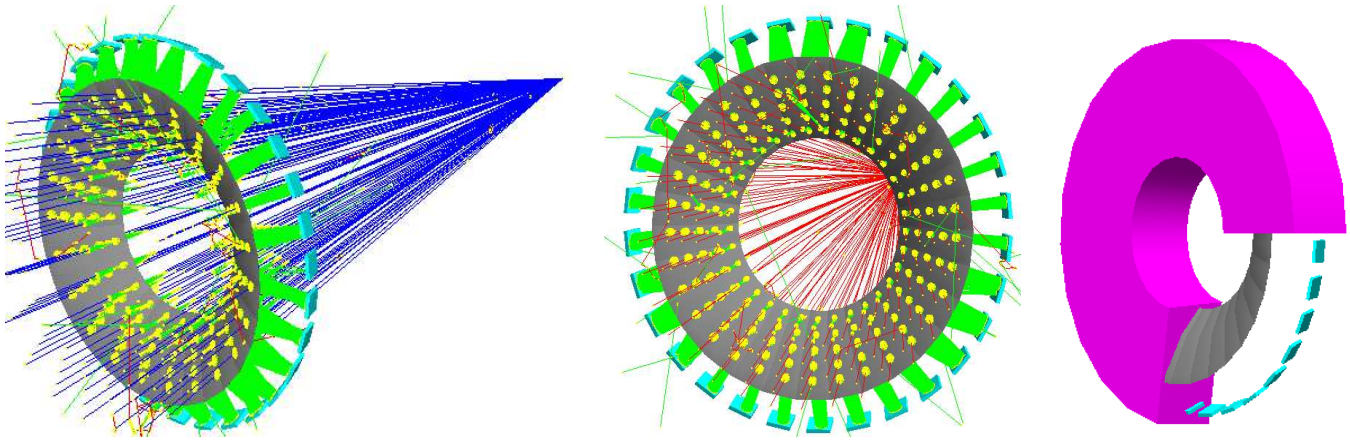

Figure 23: Optical system for the heavy-gas Cherenkov: a ring of 30 spherical mirrors (grey) will focus the Cherenkov photons (green) created by the passage of positive (left panel) and negative (center panel) pions through the C_4F_{10} radiator gas onto photon detectors (cyan). The placement of the mirrors and photon detectors in the tank (magenta) is also shown (right panel).

A Cherenkov detector filled with C_4F_{10} at 1.5 atm would be placed right after the light-gas Cherenkov to provide pion-proton/kaon separation in a momentum range from 2.2 to 7.6 GeV. A GEANT4 simulation is underway for this detector and the same design ideas and concepts will be used as for the light-gas Cherenkov.

Figure 2 displays preliminary results from this simulation: focusing of Cherenkov light with one spherical mirror is shown for both positive (left panel) and negative pions (center panel). The photon detector size is set to be 12″ by 12″ just as for the light-gas Cherenkov. With this setup the light collection efficiency is very good for the entire kinematic range of interest.

4.5.6 Trigger Setup and DAQ

As shown in Sec. 4.4, the single rate in this experiment will be about factor 5-10 lower than the sister experiment with a polarized ^{3}He target [108, 112]. Therefore, the design of trigger setup and DAQ of the ^{3}He experiment will satisfy our needs in this setup.

4.6 Beamline Instrumentation

4.6.1 Beam Chicane

In this experiment the polarization direction of the proton target will be held transverse to the beam direction. The strong magnetic field of the target will create a non-negligible deflection of the electron beam. To ensure the proper transport of the beam into the downstream exit beam pipe, a chicane will be employed. Two chicane magnets will be used for this purpose. The first one will be located 10m upstream of the target and this will bend the beam out of the horizontal plane to vertically down. The second magnet which will be located about 4m upstream of the target will bend back the beam at an angle that will compensate the 5 Tesla target field. We will choose the bend angle such that the beam will pass through the exit beam pipe after interacting with the target. A

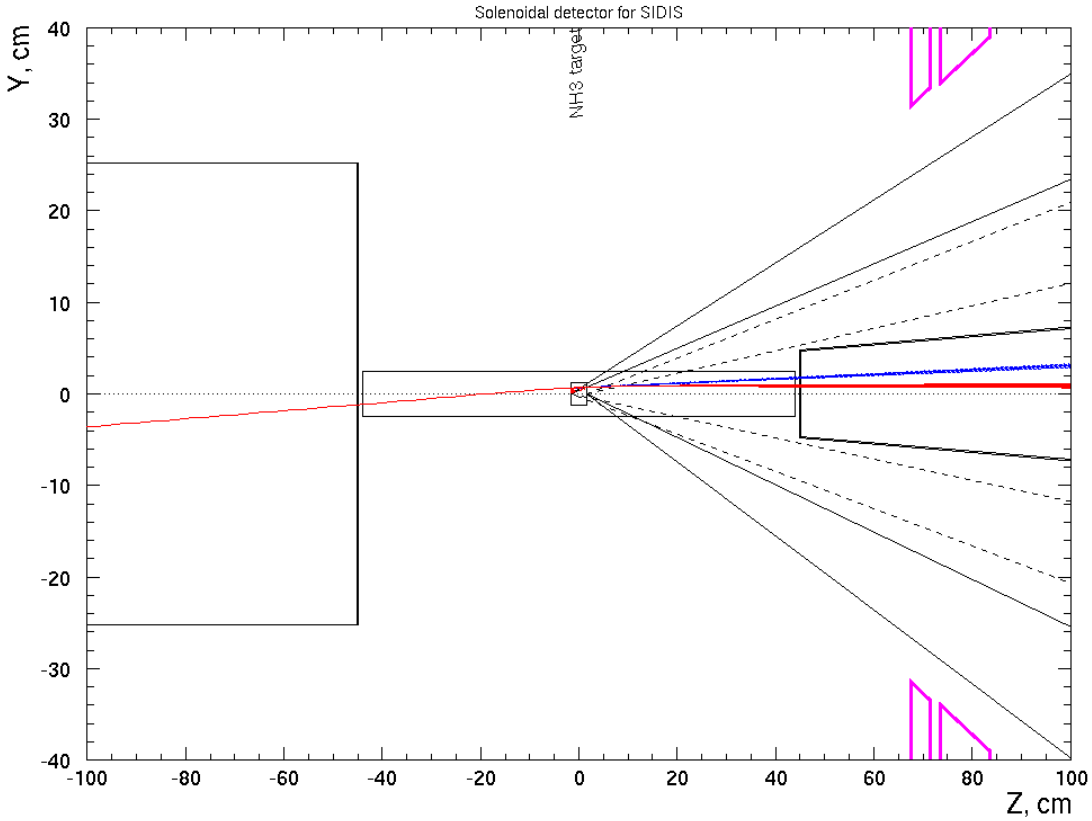

Figure 24: Event display of the beam transport at the target region with the initial bend of the beam before hitting the target. The red color denotes the 11 GeV beam and the blue color denotes the uncharged particles (mostly bremsstrahlung photons). The NH_3 target field direction is pointing into the page.

GEANT3 simulation was performed to optimize the bend angle. The simulations included physics processes such as synchrotron radiation and Bremsstrahlung. Fig. 24 shows an event display for the 11 GeV beam. Beam position monitors will be used before and after the chicane for the proper transport of the beam. They will also be used in determining the beam positions at the target.

4.6.2 Beam Charge Monitors

Typically low beam currents (up to 100 nA) are used for the polarized proton target to reduce the depolarization effects and any significant changes to the density. The standard Hall-A BCM cavities are linear down to 1 μ A. An upgrade of the beam diagnostic elements such as BCM, BPM and Harps are planned for the g2p experiment (E08-028) in Hall-A, which uses the polarized proton target, and is scheduled to run in Oct 2011. The planned upgrade will allow us to measure the beam charge and positions up to 50 nA current. In order to calibrate the beam charge a tungsten calorimeter will be used. This device is also being refurbished and will be used in Hall-A during winter 2011 running. Tungsten

calorimeter can provide an absolute calibration of Hall A BCM with an accuracy of better than 2%.

4.6.3 Slow and Fast Raster

Along with the existing Hall-A faster raster we will use a slow raster just upstream of the target. The fast raster will have a 2 mm x 2 mm pattern and the slow raster will cover a circle of 20 mm diameter. This is done in order to uniformly cover most of the surface of the target cell which has a 25 mm diameter.

5 Systematics

To achieve the proposed precision, it is very important to control the systematic uncertainties. The large azimuthal angular coverage plays an important role in reducing the experimental systematic uncertainties. The large signal-to-noise ratio will also help to reduce the systematic uncertainties in subtracting backgrounds.

5.1 Target spin flip

To minimize systematic uncertainty, frequent target spin reversal is necessary. Due to the strong target magnetic field (5T), it is difficult to rotate the target field direction to realize the spin reversal. The practical method is to use RF spin flip with the adiabatic-fast-passage (AFP) technique. There was an extensive study done by Haulte *et al.* [119] many years ago. It was shown that with ^{7}LiH, the efficiency of AFP spin flip reached up to 90%. ^{7}LiH, with its excellent radiation resistance and high dilution factor, could be a good candidate as a target material. No extensive study has been done yet on NH_3. Studies are planned in the near future both for the SSA in SIDIS and for SSA in polarized Drell-Yan experiments. The most current information on the efficiency of AFP spin-flip for NH_3 is in a proceedings paper from a recent workshop [120] in which it is expected to be about 50% for the condition at 5T/1K. With its spin-up (recovering) time of about 20 minutes, if we keep the spin flip frequency to be every two-hour, the net effect will be a loss of about 10% of the polarization. Combining the spin-flip effect together with the beam depolarization, the average in-beam polarization with spin flip will be roughly 70% with a 2-hour interval of spin flip.

5.2 The experimental observable

In this experiment, we will form the target SSA $A^h_{UT}(\phi_h, \phi_S)$ directly from the luminosity-normalized yield:

$$A^h_{UT}(\phi_h, \phi_S) = \frac{1}{(p_T)} \cdot \frac{N_1(\phi_h, \phi_S) - N_2(\phi_h, \phi_S + \pi)}{N_1(\phi_h, \phi_S) + N_2(\phi_h, \phi_S + \pi)} \tag{24}$$

The relative luminosity was monitored by various spectrometer singles rates and the downstream luminosity monitors. In addition, the target spin will be flipped every one hour with an relative polarization loss of 10%.

5.3 Raw Asymmetry

From Eq. 24, the major systematic uncertainties are from time-dependent luminosity, acceptance, polarization and detector efficeincy. The time-independent part of these uncertainties will be cancelled in the first order. In general, the time-dependent part of luminosity/acceptance/detector efficiency can be monitored using single's electron/pion rates as well as luminosity monitors. We expect to control the systematic uncertainties to be less than 2% in each pair. With a 2-hour spin flip rate, we will have 1000 pairs of spin flip in 82.5 days of running with transversely polarized target. Then the systematic

uncertainties for the raw asymmetry is about $2.0\%/\sqrt{1000}$ about 6.3e-4 level, which is much smaller than the average statistical uncertainties 2e-3.

The second one is the systematic uncertainty corresponding to the knowledge of the target polarization. The knowledge on the target polarization is at 3% level, which will give a 3% relative uncertainty.

The third one is the systematic uncertainty corresponding to the knowledge of the target polarization direction. The knowledge on this direction is about 0.2°. The effect on each asymmetry can be estimated as $1-\cos(\Delta\theta) \approx \frac{\Delta\theta^2}{2} \approx 1e-5$. (relative) The knowledge of the electron scattering azimuthal angle is also about 0.2°. The largest effect is on the pretzelosity asymmetry which is about $1-\cos(2\Delta\theta) \approx \frac{4\Delta\theta^2}{2} \approx 4e-5$. (relative) The combined effect of these two angles will not bigger than $1e-4$ (relative). In addition, the effect of the asymmetry mixing due to the inaccuracy of the two angles is negligible due to the integration over them (ϕ_h and ϕ_S).

5.4 Incomplete Azimuthal Angular Coverage

As stated in the experimental sections, the lines of flames will lead to a much higher background on certain regions of our detectors. We have to disable or remove those detectors as indicated in Fig. 9. This would result an incomplete azimuthal angular coverage in ϕ_h and ϕ_S, as shown in Figs. 14,17,15,17. The incomplete coverage in azimuthal angular coverage would lead to an reduction of statistical precision of each terms (Collins/Sivers/pretzlosity) fitted from the azimuthal angular coverage. Such reduction is well understood as illustrated in the appendix of E12-10-006 proposal. We include this reduction factor in precisions in our projections through the generated ϕ_h vs. ϕ_s coverage through GEANT3 simulation.

5.5 Azimuthal Angular Asymmetry in A_{UL}

In the lab frame, when the ^3He is transversely polarized with respect to the beam direction. However, in the definition of A_{UT}, the S_T is defined as the transverse polarization with respect to the virtual photon direction, which has a small angle with the z-axis. Therefore, there will be a small S_L component. When the target spin is flipped, The S_L will also flip. Thus there will be a false asymmetry from the S_L contamination. The average S_L values are 0.1 and 0.15 with 11 GeV and 8.8 GeV incident beam energies, respectively. Dedicated data (4 days) will be taken with a longitudinally polarized target to measure the A_{UL} directly.

5.6 Dilution Factors

For the target dilutions studies we will take several different sets of data including empty cell (with ^{4}He/windows/shielding etc.) runs and solid target runs such as ^{12}C and CH_2. Typically, with this target, ^{12}C data is used to approximate the nitrogen contributions. The packing factor and dilutions can be studied with both elastic as well as DIS settings. There were many studies done on the extraction of packing factor/dilution factor from the previous experiments (E143, E155, E155x, GEn-I and GEn-II, RSS and SANE).

5.7 Higher Twist effect

The higher twist effects will be studied in the approved experiment [108] using the unpolarized Hydrogen and Deuterium data from the factorization test. In addition, one important feature for the single-target spin asymmetry is that some of the higher twist terms have different azimuthal angular dependence. In this case, a direct fitting of the data with more azimuthal angular dependence terms provide a direct measure of the higher twist data.

5.8 Systematic Uncertainty Budget

The systematic uncertainties are summarized in Table. 3.

Sources	Type	Collins π^+	Collins π^-	Sivers π^+	Sivers π^-
Raw asymmetry	absolute	6.5E-3	6.5E-3	6.5E-3	6.5E-3
Background Subtraction	relative	0.1%	0.1%	0.1%	0.1%
Diffractive Vector Meson	relative	3%	2%	3%	2%
Radiative Correction	relative	2%	2%	2%	2%
Target Polarization	relative	3% +0.5%	3% + 0.5%	3% +0.5%	3% + 0.5%

Table 3: Systematic uncertainties on the separated asymmetries for the proposed experiment. The average statistical uncertainties on the separated asymmetries will be around 1.4e-2 (absolute) with 674 bins.

6 Beam Time Request and Projections

6.1 Beam time request

The beam time request is listed in Table 3. We request 94 days of total beam time with 100 nA, 11/8.8 GeV electron beams on a 3-cm (0.5 cm) long, polarized NH_3 target. The 8.8 GeV beam energy will provide precision data on the radiative corrections along with the increased Q^2 coverage. 90 days are for beam on a transversely polarized NH_3 target including, and 7.5 days for dilution measurements, optics, and detector calibrations. We also request 4 days with a longitudinal target polarization to study the systematics of A_{UL} contamination. Although beam polarization is not required for the proposed SSA measurements, we request a longitudinally polarized beam for a parasitic measurement of the A_{LT} which can be used to access another leading twist distribution, g_{1T}. In addition, there will be an overhead time of 26 days for regular target annealing which does not need an electron beam. This overhead time can be shared with other regular activities such as detector maintenance, etc. Some of this target annealing activities can also be arranged to coincide with the scheduled accelerator maintenance activities in order to reduce overhead time.

	Time (Hour)	Time (Day)
Trans. Pol. NH_3 at 11 GeV	**1320**	55
Trans. Pol. NH_3 at 8.8 GeV	**660**	27.5
Longi. Pol. NH_3 at 11 GeV	60	2.5
Longi. Pol. NH_3 at 8.8 GeV	36	1.5
Dilution measurements	36	1.5
optics and detector calibration	144	6
Target Overhead regular annealing	624	26
Total Time Request	**2256+624**	**94+26 days**

Table 4: Details of the beam time request.

6.2 Projections

The projections combine both 11 GeV data and 8.8 GeV data. All projections were done after taking into account the partial loss in the azimuthal coverage due to "line of flames" and details about taking into account the acceptance effect are given in Appendix A. Both the dilution factor and packing fraction have been taken into account in projecting the proposed measurements. The projected results for π^+ Collins, Sivers, and pretzelosity asymmetries at one typical kinematic bin, $0.45 > z > 0.4$, $3 > Q^2 > 2$, are shown in Fig. 25, Fig. 26, Fig. 27, respectively. The corresponding projections for the π^- asymmetries are shown in Fig. 28, Fig. 29, Fig. 30. The x-axis is x_{bj}. The y-axis on the left side is P_T which is the transverse momentum. The y-axis on the right side shows the scale

of the asymmetry. The y-position of the projections shows the average P_T value for the corresponding kinematic bin. The statistical uncertainties follow the scale on the right side of y-axis. The scale of the theoretical calculations follow the right side y-axis. Also shown in these figures are data from the HERMES and COMPASS (proton) collaborations, and theoretical predictions from Anselmino *et al.* [93], Ma *et al.* [126], Pasquini [60] and Vogelsang and Yuan [127] for the Collins asymmetry. For prezelosity projections, we show theoretical predictions from Ma *et al.* [103], Pasquini [60], and we show predictions from Anselmino *et al.* [86, 104] for the Sivers case together with its model uncertainty.

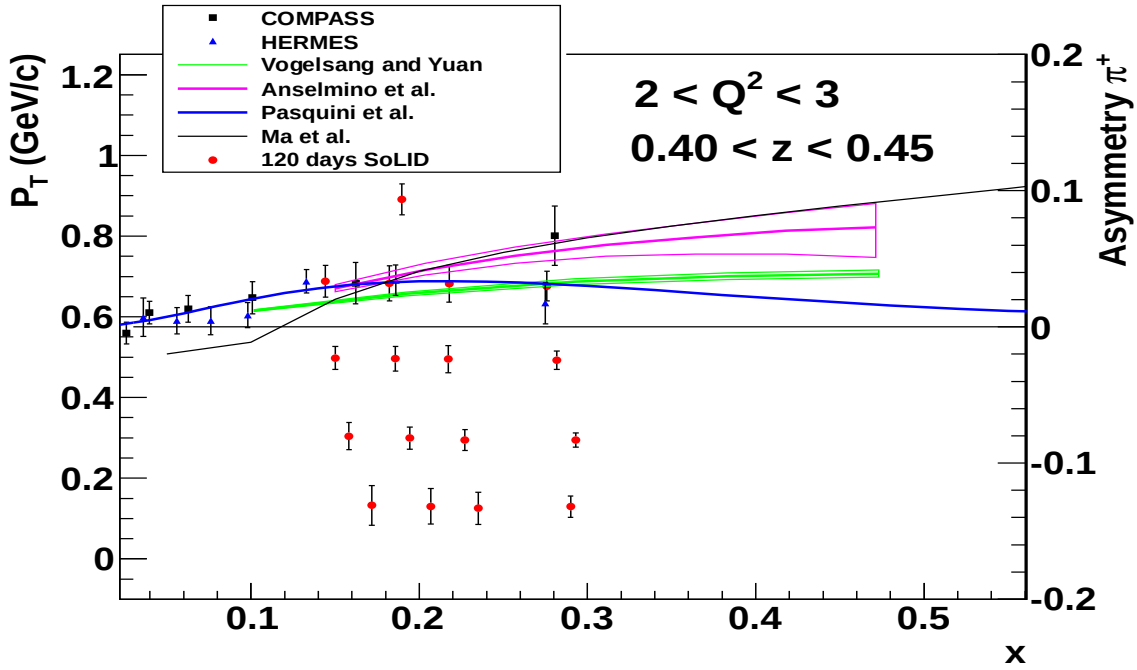

Figure 25: 12 GeV Projections with SoLID and a transversely polarized NH_3 target for π^+ Collins asymmetries at $0.45 > z > 0.4$, $3 > Q^2 > 2$.

The complete projections for π^+ Collins/Sivers/pretzelosity asymmetries are shown in terms of 4-D (x, z, P_T and Q^2) kinematic bin in Fig. 31, Fig. 32, and Fig. 33. Theoretical predictions from same groups as discussed previously are shown in the first panel only for better visibility. The Q^2 and z values for these calculations are the average value of the entire kinematics. The x-dependence of asymmetries in different z bins is shown in different panels. The corresponding complete projections for π^- Collins, Sivers and pretzelosity asymmetries are shown in terms of 4-D (x, z, P_T and Q^2) kinematic bin in Fig. 34, Fig. 35, and Fig. 36.

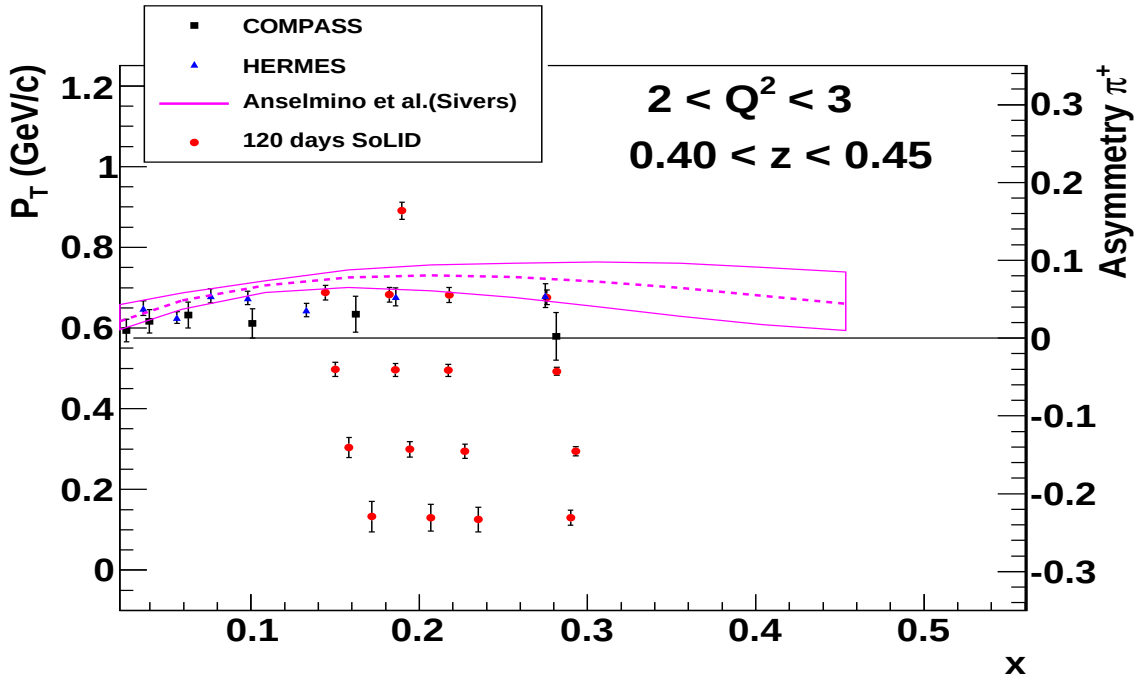

Figure 26: 12 GeV Projections with SoLID and a transversely polarized NH_3 target for π^+ Sivers asymmetries at $0.45 > z > 0.4$, $3 > Q^2 > 2$.

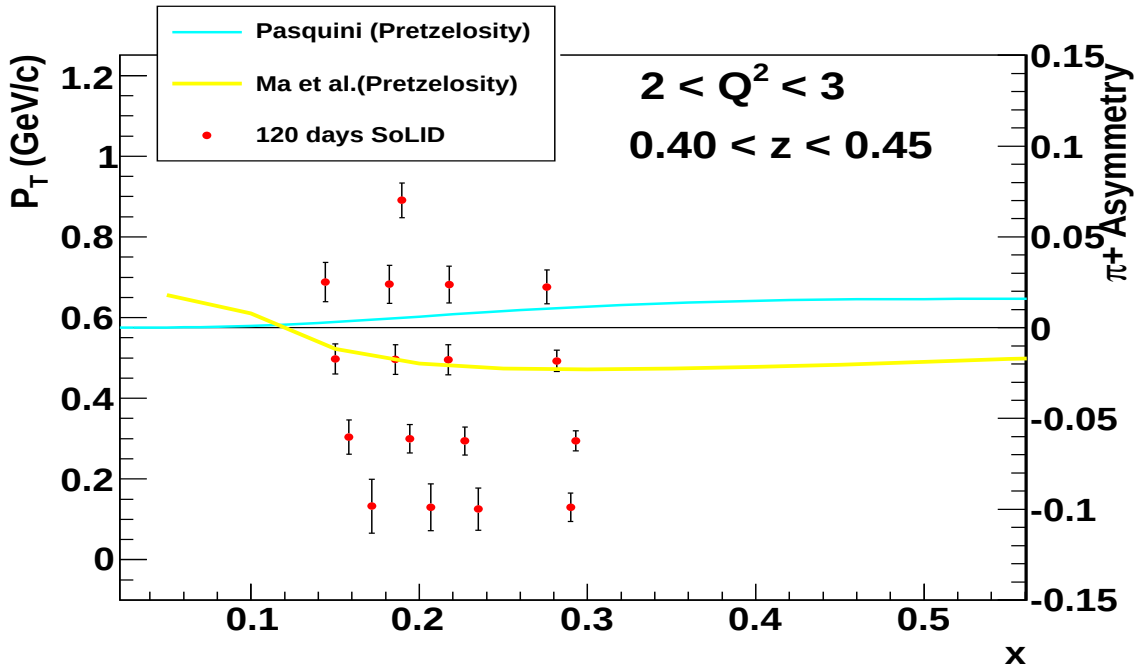

Figure 27: 12 GeV Projections with SoLID and a transversely polarized NH_3 target for π^+ pretzelosity asymmetries at $0.45 > z > 0.4$, $3 > Q^2 > 2$.

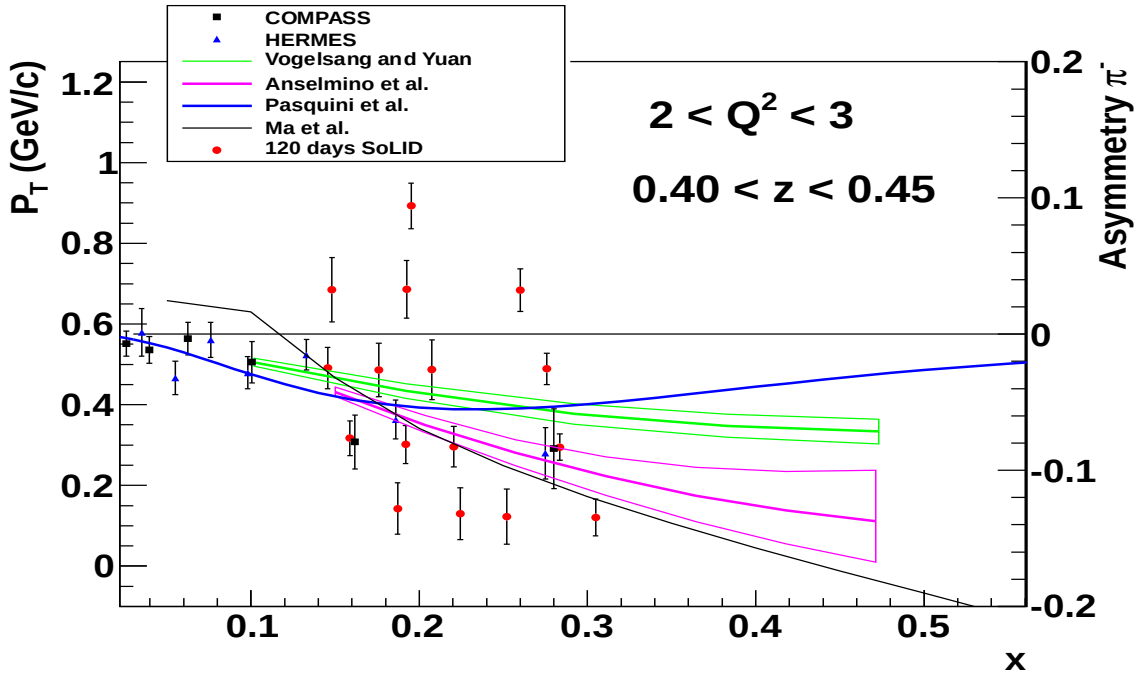

Figure 28: 12 GeV Projections with SoLID and a transversely polarized NH_3 target for π^- Collins asymmetries at $0.45 > z > 0.4$, $3 > Q^2 > 2$.

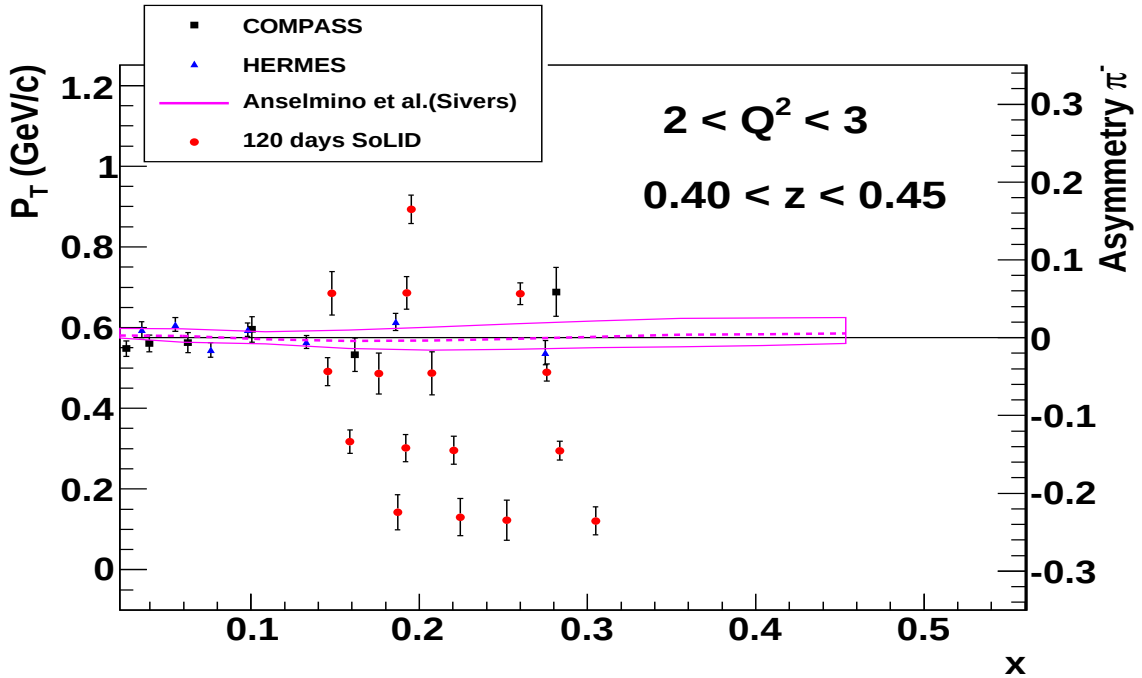

Figure 29: 12 GeV Projections with SoLID and a transversely polarized NH_3 target for π^- Sivers asymmetries at $0.45 > z > 0.4$, $3 > Q^2 > 2$.

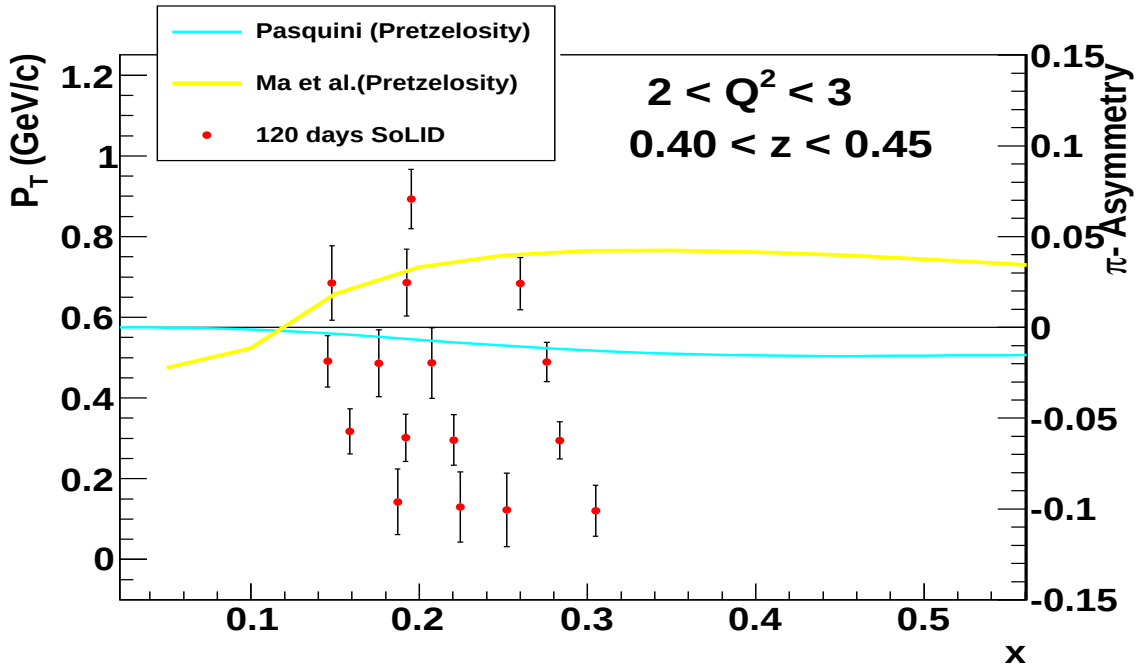

Figure 30: 12 GeV Projections with SoLID and a transversely polarized NH_3 target for π^+ pretzelosity asymmetries at $0.45 > z > 0.4$, $3 > Q^2 > 2$.

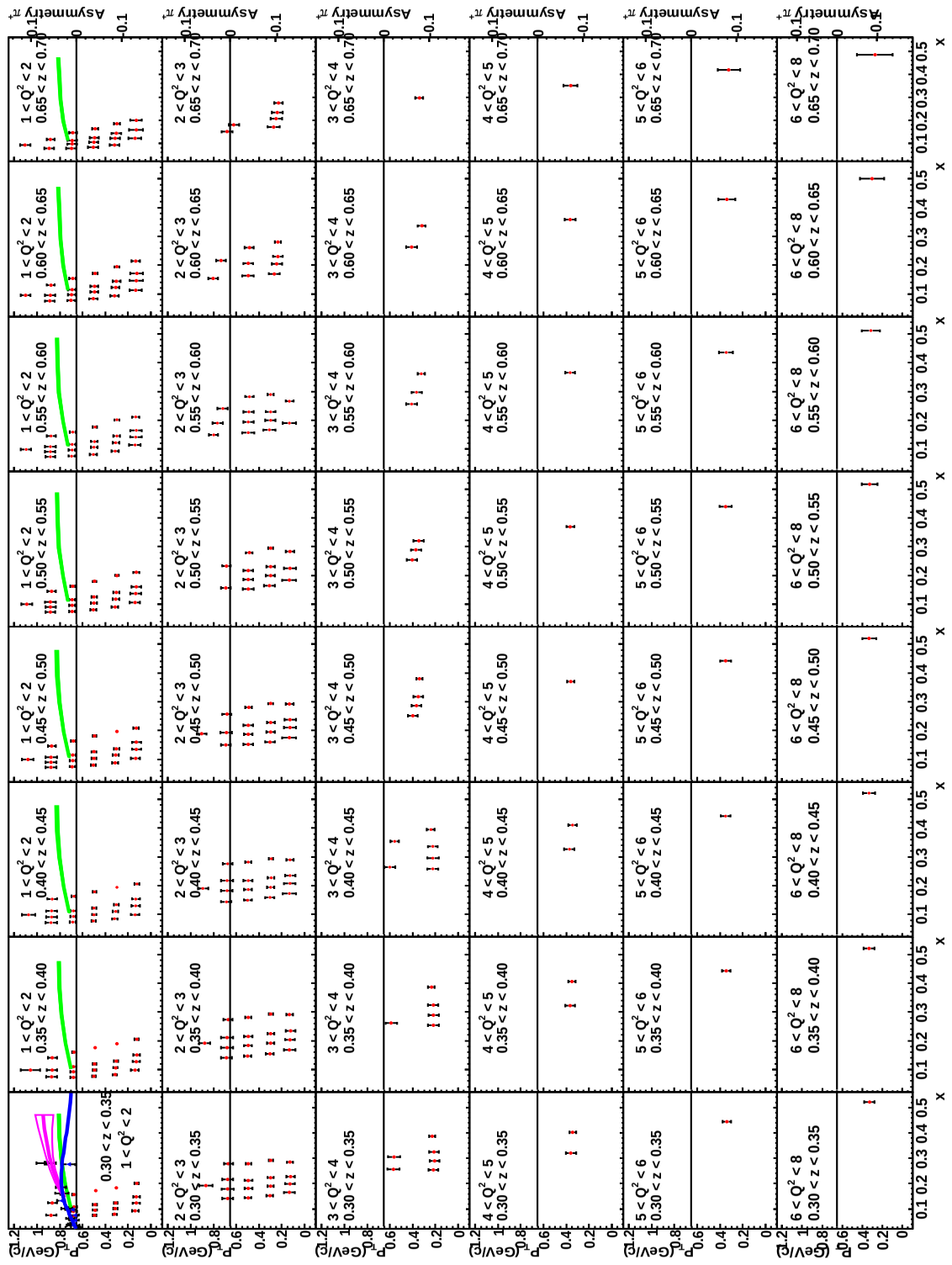

Figure 31: 12 GeV Projections with SoLID and a transversely polarized NH_3 target for the π^+ Collins asymmetries for all kinematic bins in terms of different z and Q^2 bins.

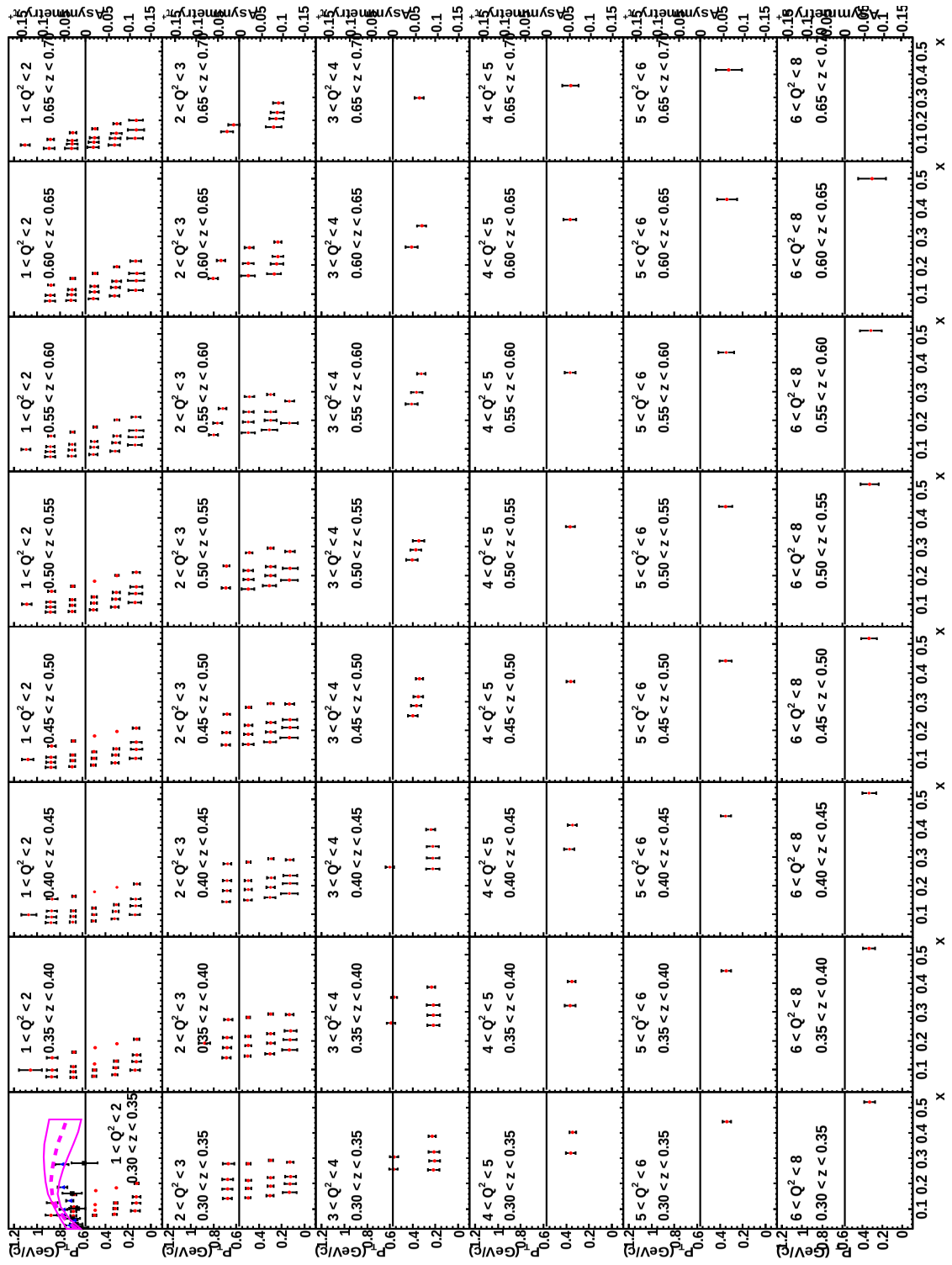

Figure 32: 12 GeV Projections with SoLID and a transversely polarized NH_3 target for the π^+ Sivers asymmetries for all kinematic bins in terms of different z and Q^2 bins.

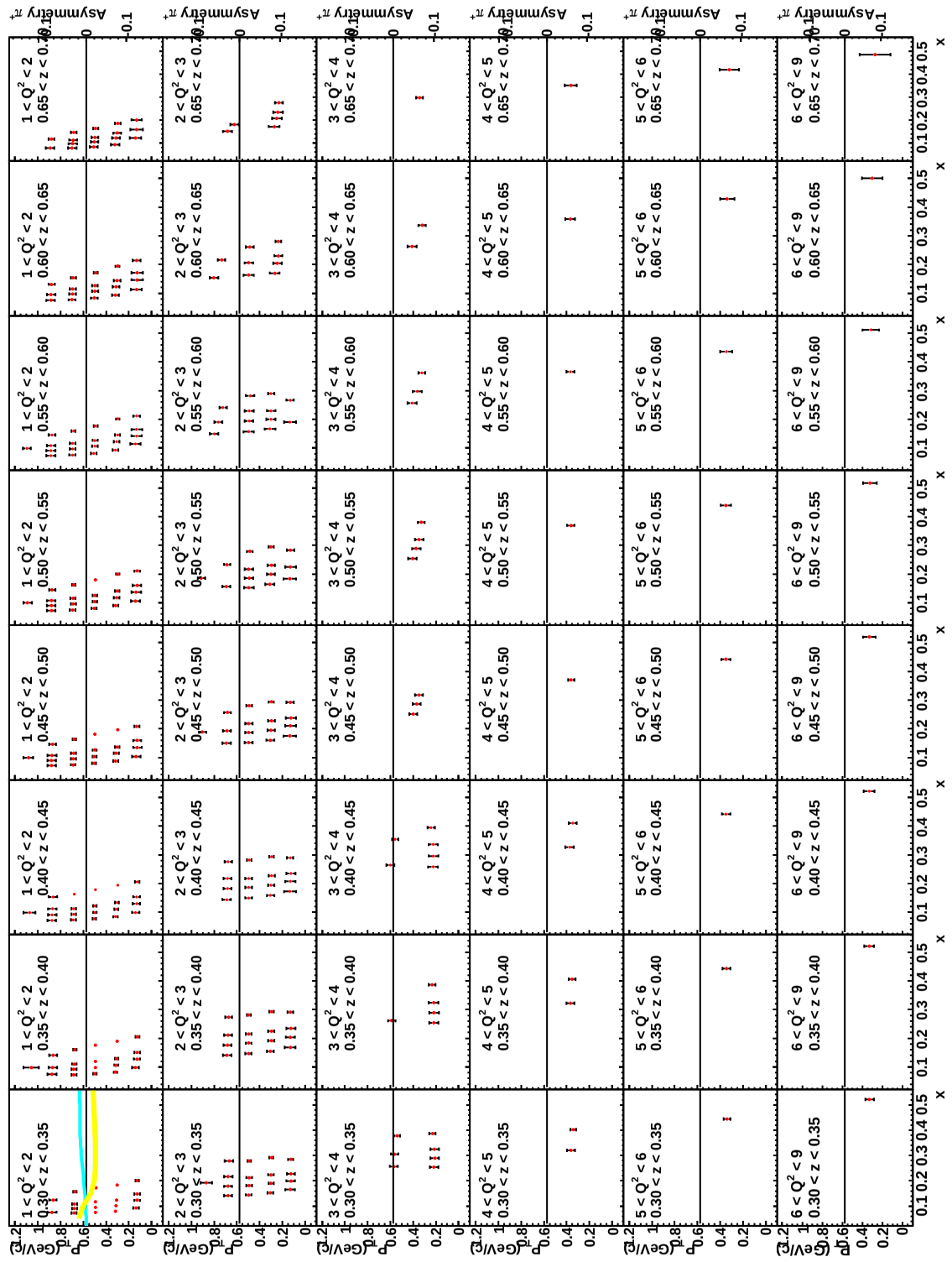

Figure 33: 12 GeV Projections with SoLID and a transversely polarized NH_3 target for the π^+ pretzelosity asymmetries for all kinematic bins in terms of different z and Q^2 bins.

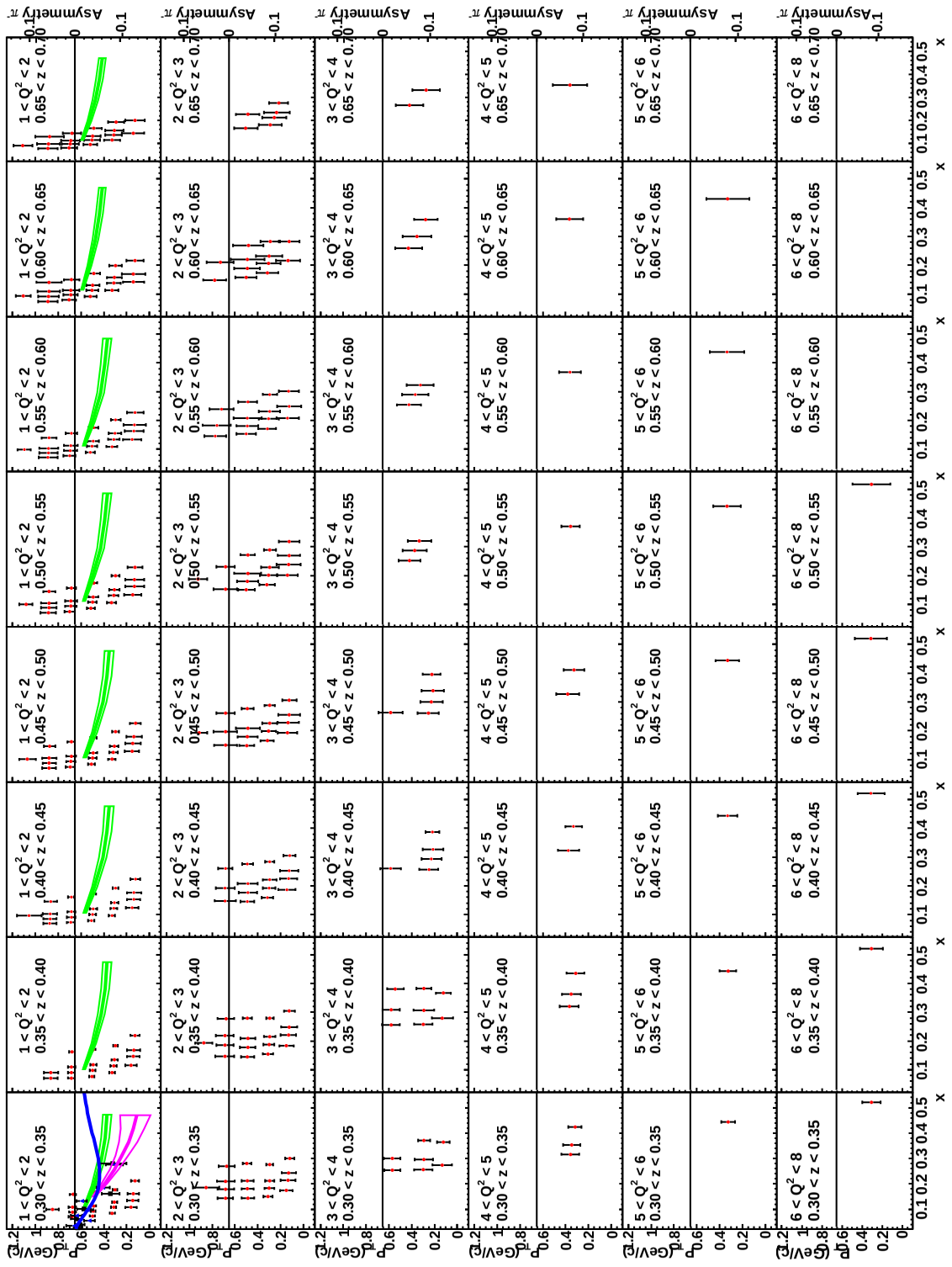

Figure 34: 12 GeV Projections with SoLID and a transversely polarized NH_3 target for the π^- Collins asymmetries for all kinematic bins in terms of different z and Q^2 bins.

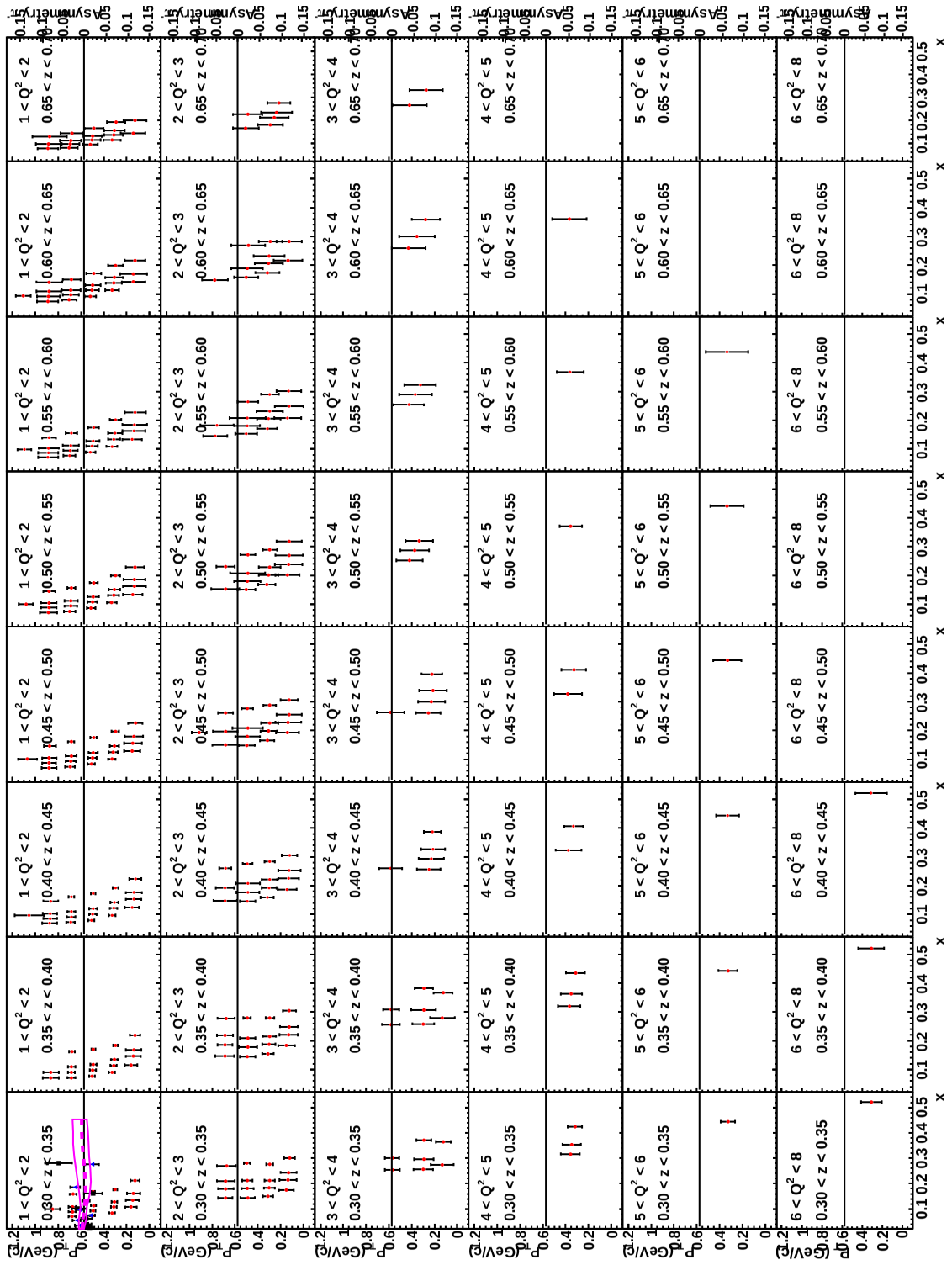

Figure 35: 12 GeV Projections with SoLID and a transversely polarized NH_3 target for the π^- Sivers asymmetries for all kinematic bins in terms of different z and Q^2 bins.

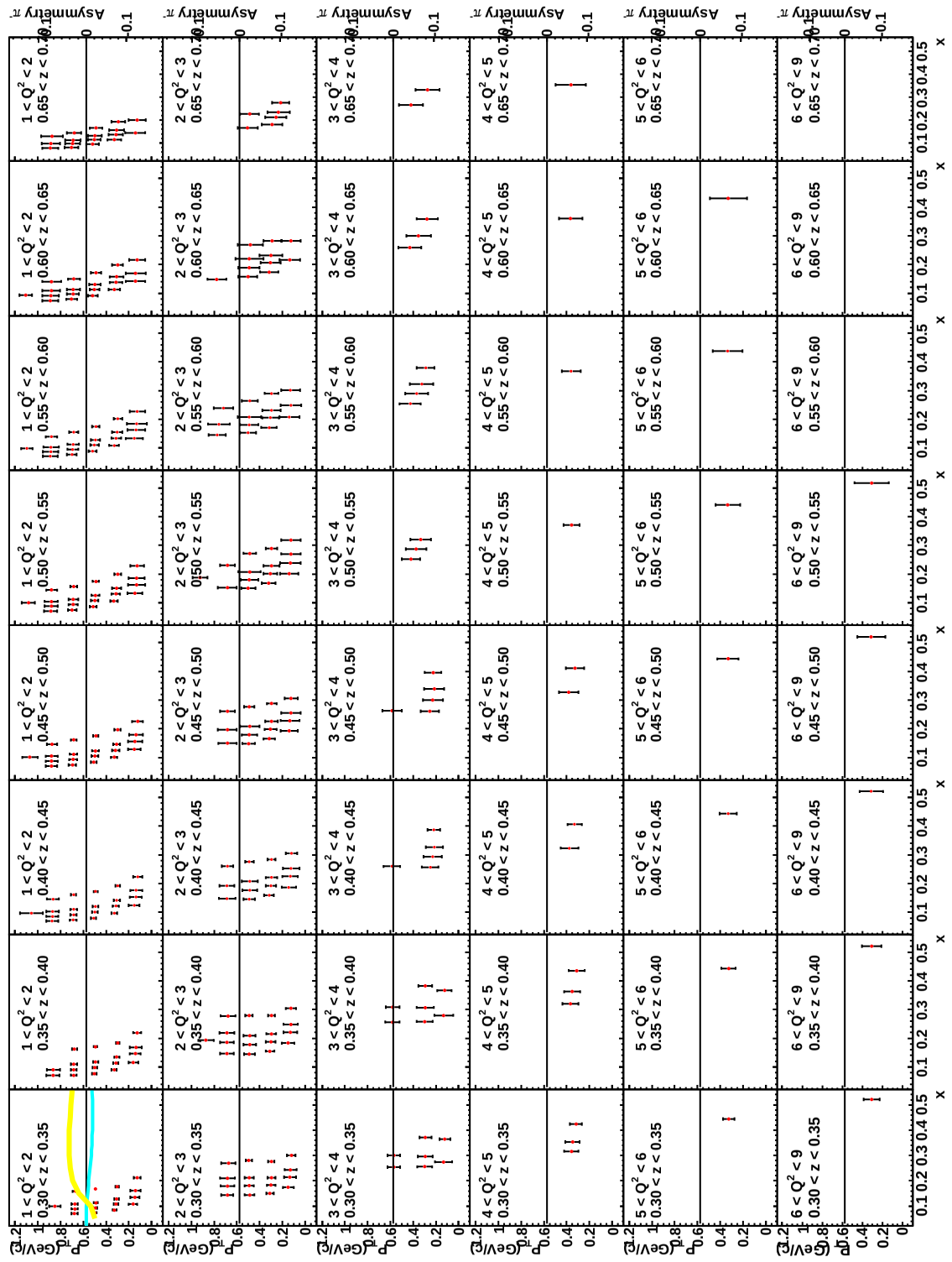

Figure 36: 12 GeV Projections with SoLID and a transversely polarized NH_3 target for the π^- pretzelosity asymmetries for all kinematic bins in terms of different z and Q^2 bins.

7 Impact of this Measurement

From the projections, we can see that the results from the proposed experiment will have great impact on the current theoretical understanding of the transverse spin physics. Firstly, we will extend the study of the SIDIS to a real 4-D manner (x, Q^2, z and P_T). Secondly, we will extend the measurement of the transversity distribution to the large x region which is essential in extracting the tensor charge. Thirdly, the Sivers distribution and pretzelosity distribution functions, which are crucial to understand the relativistic effect and the role of quark orbital angular momentum, will be mapped precisely in 4-D. Further, we will cover a large P_T region which is important in testing various theoretical approaches and modeling of the TMDs. Finally, we will cover a relatively large Q^2 region which can study higher-twist contributions [5].

Probing TMDs, in particular transversity distribution, the least known leading-twist quark distribution function, which is non-zero upon integrating over the quark transverse momentum, is among the goals of several ongoing and future experiments. The experimental study of TMDs, which is now only at its inception, promises to have a very exciting future. Understanding the TMDs for different quark flavors is certainly a complex task which demands major efforts in different laboratories in studying many different processes ranging over a wide kinematic region.

This is a fast evolving field with growing interests worldwide. It is important for JLab to be a major player in this important frontier. Measuring the transversity distribution and probing the TMDs through SIDIS at Jefferson Lab has attracted a lot of attentions by many theorists and experimentalists [108] already. A combined analysis of the proton and neutron data using the SoLID will provide the best precision in 4-d on u and d-quark TMDs and transversity distribution functions. It will have impact on other related programs and particularly on the design of future facilities with TMDs study as one of their important physics goals, for example the EIC, the FAIR project at GSI, and J-PARC. The proposed 11 GeV experiment will also help to move theory forward in understanding and in modeling the quark TMDs significantly.

A combined analysis between our proton results and the neutron results from polarized ^{3}He measurement, will be carried out to extract the tensor charge of the u and d quark. The high statistics data from both the proton and the neutron will lead to a unprecedented precise determination of tensor charge (less than 10%) in a model-independent way. Such a precision will provide important tests of Lattice QCD predictions for the tensor charge.

[5] Higher twist effects can also be observed with contributions with $\sin(\phi_S)$ and $\sin(2\phi_h - \phi_S)$ angular modulations.

8 Relations to other SIDIS experiments on TMDs

With the reach of an 11-GeV electron beam energy upon the 12-GeV energy upgrade of CEBAF, a coherent program on SIDIS is emerging at JLab which is poised to make major advancements in our understanding of partonic structure of the nucleon in terms of flavor, momentum and spin. The proposed experiment is a very important part of this overarching program. For a detailed introduction of the entire JLab SIDIS program, we refer the readers to the document prepared by H. Avakian *et al.* which was submitted to PAC37 and PAC38. In this section, we will discuss more specifically the relationship of this experiment to the other proposed SIDIS experiments with a focus on TMDs.

There are two approved SoLID SIDIS experiments on TMD physics using a high-pressure transversely (longitudinally) polarized ^{3}He target: E12-10-006 (E12-11-007). The aim of E12-10-006 is a precise measurement of Collins, Sivers and prezelosity asymmetries in a 4-D kinematic space of (Q^2, z, x, P_T) in order to access the transversity, Sivers and the pretzelosity distributions of the neutron. This experiment is complemented by E12-11-007 in which the two additional TMDs, $h_{1L}^{\perp}$ and g_{1T} will be measured with precision on the neutron. The proposed experiment is an isospin counterpart of E12-10-006 which will provide precise information on the proton in 4-D space. The combination of E12-10-006 and this experiment will allow for a flavor separation and determination of the tensor charge of the d and u quark to 10%, a precision important for crucial test of lattice QCD predictions of this intrinsic property of the nucleon.

The conditionally approved SIDIS experiment C12-09-018 in Hall A will use the Super-Bigbite spectrometer for detecting mesons and the Bigbite spectrometer for detecting the scattered electrons with an upgraded transversely polarized ^{3}He target. A RICH detector (based on the components of the HERMES' RICH is also planned to allow for the identification of kaons in addition to pions). The proposed experiment will provide precise data on the neutron as a function of x and z, integrated over P_T and Q^2. The experiment proposes two beam energies: 8.8 GeV and 11 GeV in order to have two values of Q^2 for each bin of (x, z). Further, Experiment C12-09-018 will provide data on neutral pions also. As such this experiment is complementary to our proposed experiment on the proton in which precise data will be obtained in fine binnings in the (x, z, P_T, Q^2) 4-D phase space.

Hall B has an extensive SIDIS program accessing TMDs. The program includes the approved experiments: E12-06-112, E12-07-107, E12-07-007, E12-09-009 and E12-09-008 using unpolarized and longitudinally polarized proton and deuteron targets. The planned CLAS12 program will also include charged kaon detection using a RICH detector which is anticipated to be added to the CLAS12 detection system. Therefore, the approved CLAS program on TMD physics is completely complementary to our proposed experiment. We are aware that a new proposal [128] from CLAS using a transversely polarized HDice target will be submitted to PAC38. The proposed kinematics and precision are similar to what we are proposing, though our projected figure-of-merit is a factor of 2.4 of that projected in the new CLAS proposal, and SoLID has full azimuthal coverge which is crucial for controlling the systematics. Given the importance of TMD physics, it is crucial and necessary to probe the same physics using different apparatus with different systematics. We believe both experiments should be pursued vigorously so that the 12-GeV TMD

program will be a complete success with confidence.

9 Collaboration and Responsibilities

The proposed experiment requires the SoLID apparatus which was proposed already for two approved SIDIS experiments [108, 110] and the approved PVDIS experiment [111]. The SoLID apparatus consists of a solenoid magnet with a field strength of 1.5 Tesla and various detectors for charged particles detections. The PVDIS experiment requires the same device with a slightly different configuration regarding the target and the detectors. Since the approval of these experiments, the SIDIS and the PVDIS collaborations have formed the SoLID collaboration and have studied a number of different options for a solenoid magnet. The conclusion based on the physics impact of both programs and the likelihood of getting a magnet is that the CLEO-II magnet is the preferred choice to pursue for SoLID. The SoLID collaboration will work closely with JLab management and DOE in securing this magnet. The PVDIS experiment [111] will require GEM detectors for tracking, an electromagnetic calorimeter and gas Cerenkov counter for trigger and electron identification. The SIDIS experiments will require in addition to the aforementioned detectors: a heavy gas Cerenkov detector and a MRPC TOF detector for charge pion identifications. The SoLID collaboration will work closely with JLab in securing funding for the construction of various detectors. A stronger Chinese collaboration has formed since the PAC35 approval of E12-10-006 experiment [108, 110]. The Chinese collaboration has taken on the major responsibilities of the GEM detector with CIAE, Lanzhou. USTC, Tsinghua being the major players in this effort. Tsinghua University has also taken on the major responsibility of the construction of the MRPC TOF for SIDIS. The Chinese collaboration is also actively applying for funding from the National Science Foundation of China, Ministry of Science and Technology and Chinese Academy of Sciences for the construction of the GEM detectors. For a more detailed breakdown of responsibilities of leading institutions in the collaboration, we refer to PAC34 proposal [109].

10 Summary

We are proposing a precise measurement of SSA from semi-inclusive electroproduction of charged pions from a transversely polarized proton target in DIS region. The proposed experiment will provide precise 4-D (x, Q^2, z and P_T) data on the Collins, Sivers and pretzelosity asymmetries on the proton. In particular, the Collins asymmetry on the proton will provide direct information about the tensor charge. These data together with the results from a transversely polarized "neutron" (^{3}He) target in a similar x region will enable a model-independent determination of the u and d quark tensor charge. The projection of the proposed experiment is to reach a less 10% relative precision on the u/d quark tensor charge. Such a precision will allow for a meaningful test of lattice QCD predictions of this intrinsic property of the nucleon. To carry out the experiment, we will use the approved SoLID spectrometer and a transversely polarized NH_3 target. We request a total number of 120 days of beam time at incident electron beam energies of 11/8.8 GeV.

Appendix A: Estimation of Statistical Uncertainties

In the estimation of statistical uncertainties, the Collins, Sivers and pretzelosity asymmetries need to be estimated separately. The separated statistical uncertainties depend on the acceptance, azimuthal angular coverage, detection efficiency, the number of events in each kinematic bin, and the number of terms used in the fitting procedure. In the projected results, we only consider the leading twist contributions (Collins, Sivers, and pretzelosity) in the fitting procedure. In this experiment, the acceptance is no longer flat because of the cuts to remove the "line of flame" and the deflection of charged particles in the target field. The formalism includes the acceptance effect is described in this section. In general, the transverse single target spin asymmetry can be written in leading twist as:

$$\begin{aligned} A_{UT} &= A_{Sivers} sin(\phi_h - \phi_s) + A_{Collins} sin(\phi_h + \phi_s) + A_{Pretzelosity} sin(3\phi_h - \phi_s) \\ &= a sin(\phi) + (b+c) sin(2\phi_h) cos\phi + (c-b) cos(2\phi_h) sin(\phi) \end{aligned} \quad (25)$$

where $\phi \equiv \phi_h - \phi_s$ is the Sivers angle, a, b and c represent Collins, Sivers and pretzelosity asymmetries, respectively. For generated events in our simulations, the coverage for both ϕ_h and ϕ_s is 2π. However, the output event distribution is uneven due to the acceptance effect. We define $g(\phi_i, \phi_{h,j}) = N_{i,j}/N_{mean}$ as the acceptance factor, where $N_{i,j}$ and N_{mean} are the corresponding accepted and generated events for each kinematic bin. We then multiply $sin(\phi)g(\phi_i, \phi_{h,j})$, $sin(2\phi_h - \phi)g(\phi_i, \phi_{h,j})$, and $sin(2\phi_h + \phi)g(\phi_i, \phi_{h,j})$ to both sides of Eqn. 25, we have

$$\begin{aligned} I_1 &= \int_{2\pi}\int_{2\pi} A_{UT} sin(\phi) g(\phi, \phi_h) d\phi d\phi_h \\ &= \int_{2\pi}\int_{2\pi} (a sin(\phi) + b sin(2\phi_h - \phi) + c sin(2\phi_h + \phi)) sin(\phi) g(\phi, \phi_h) d\phi d\phi_h \\ I_2 &= \int_{2\pi}\int_{2\pi} A_{UT} sin(2\phi_h) cos(\phi) g(\phi, \phi_h) d\phi d\phi_h \\ &= \int_{2\pi}\int_{2\pi} (a sin(\phi) + b sin(2\phi_h - \phi) + c sin(2\phi_h + \phi)) sin(2\phi_h) cos(\phi) g(\phi, \phi_h) d\phi d\phi_h \\ I_3 &= \int_{2\pi}\int_{2\pi} A_{UT} cos(2\phi_h) sin(\phi) g(\phi, \phi_h) d\phi d\phi_h \\ &= \int_{2\pi}\int_{2\pi} (a sin(\phi) + b sin(2\phi_h - \phi) + c sin(2\phi_h + \phi)) cos(2\phi_h) sin(\phi) g(\phi, \phi_h) d\phi d\phi_h \end{aligned}$$

These equations can be rewritten into matrix format:

$$\begin{pmatrix} I_1 \\ I_2 \\ I_3 \end{pmatrix} = M \begin{pmatrix} a \\ b \\ c \end{pmatrix}$$

$$M = \int_{2\pi}\int_{2\pi} S g(\phi, \phi_h) d\phi d\phi_h \quad (26)$$

$$S = \begin{pmatrix} sin^2(\phi) & sin(\phi) sin(2\phi_h - \phi) & sin(\phi) sin(2\phi_h + \phi)) \\ sin(\phi) sin(2\phi_h) cos(\phi) & sin(2\phi_h - \phi) sin(2\phi_h) cos(\phi) & sin(2\phi_h + \phi)) sin(2\phi_h) cos(\phi) \\ sin(\phi) cos(2\phi_h) sin(\phi) & sin(2\phi_h - \phi) cos(2\phi_h) sin(\phi) & sin(2\phi_h + \phi) cos(2\phi_h) sin(\phi) \end{pmatrix}$$

where M is defined as the coefficient matrix of (a, b, c), and the acceptance factor $g(\phi_i, \phi_{h,j})$ is obtained according to from simulations. We can obtain the results of the asymmetries by inverting the coefficient matrix M, if we assume:

$$M^{-1} = \begin{pmatrix} a_{11} & a_{12} & a_{13} \\ a_{21} & a_{22} & a_{23} \\ a_{31} & a_{32} & a_{33} \end{pmatrix} \tag{27}$$

Then the separated asymmetries can be written as:

$$\begin{aligned} a &= \int_{2\pi}\int_{2\pi} A_{UT}(a_{11}sin(\phi) + a_{12}sin(2\phi_h)cos(\phi) + a_{13}cos(2\phi_h)sin\phi)d\phi d\phi_h \\ b &= \int_{2\pi}\int_{2\pi} A_{UT}(a_{21}sin(\phi) + a_{22}sin(2\phi_h)cos(\phi) + a_{23}cos(2\phi_h)sin\phi)d\phi d\phi_h \\ c &= \int_{2\pi}\int_{2\pi} A_{UT}(a_{31}sin(\phi) + a_{32}sin(2\phi_h)cos(\phi) + a_{33}cos(2\phi_h)sin\phi)d\phi d\phi_h \end{aligned}$$

Thus:

$$\delta a = \sqrt{\int_{2\pi}\int_{2\pi} [\delta A_{UT}(a_{11}sin(\phi) + a_{12}sin(2\phi_h)cos(\phi) + a_{13}cos(2\phi_h)sin\phi)]^2 d^2\phi d^2\phi_h} \tag{28}$$

$$\delta b = \sqrt{\int_{2\pi}\int_{2\pi} [\delta A_{UT}(a_{21}sin(\phi) + a_{22}sin(2\phi_h)cos(\phi) + a_{23}cos(2\phi_h)sin\phi)]^2 d^2\phi d^2\phi_h} \tag{29}$$

$$\delta c = \sqrt{\int_{2\pi}\int_{2\pi} [\delta A_{UT}(a_{31}sin(\phi) + a_{32}sin(2\phi_h)cos(\phi) + a_{33}cos(2\phi_h)sin\phi)]^2 d^2\phi d^2\phi_h} \tag{30}$$

The statistical uncertainties of separated asymmetries can be estimated by these formulae, which include the acceptance effect.

References

[1] F. Caola, S. Forte, and J. Rojo, arXiv:hep-ph/1007.5405 (2010).

[2] J.P. Ralston and D. E. Soper, Nucl. Phys. **B152**, 109 (1979).

[3] D.W. Sivers, Phys. Rev. **D41** 83 (1990).

[4] A. Kotzinian, Nucl. Phys. **B441** 234248 1995.

[5] P.J. Mulders and R. D. Tangerman, Nucl. Phys. **B461** 197237 (1996).

[6] D. Boer and P.J. Mulders, Phys. Rev. **D57** 57805786 (1998).

[7] P.J. Mulders and J. Rodrigues, Phys. Rev. **D63** 094021 (2001).

[8] A.V. Belitsky, X.D Ji, and F. Yuan, Phys. Rev.**D69** 074014 (2004).

[9] A. Bacchetta et al., JHEP, **02** 093 (2007).

[10] M. Burkardt, Phys. Rev.,**D62** 071503 (2000).

[11] K. Goeke, Maxim V. Polyakov, and M. Vanderhaeghen, Prog. Part. Nucl. Phys., **47** 401-515 (2001).

[12] M. Burkardt, Int. J. Mod. Phys. **A18** 173-208 (2003).

[13] M. Diehl, Phys. Rept.**388** 41-277 (2003).

[14] X. Ji, Ann. Rev. Nucl. Part. Sci. **54** 413-450 (2004).

[15] A.V. Belitsky and A.V. Radyushkin, Phys. Rept.**418** 1-387 (2005).

[16] S. Boffi and B. Pasquini, Riv. Nuovo Cim.**30** 387 (2007).

[17] X.D Ji, Phys. Rev. Lett. **91** 062001 (2003).

[18] S.J. Brodsky, D.S Hwang, and I. Schmidt, Phys. Lett.**B530** 99-107 (2002).

[19] S.J. Brodsky, D.S Hwang, and I. Schmidt, Nucl. Phys. **B642** 344-356 (2002).

[20] J.C. Collins, Phys. Lett. **B536** 43-48 (2002).

[21] X.D. Ji and F. Yuan, Phys. Lett. **B543** 66-72 (2002).

[22] A.V. Belitsky, X. Ji, and F. Yuan, Nucl. Phys. **B656** 165-198 (2003).

[23] D. Boer, P.J. Mulders, and F. Pijlman, Nucl. Phys. **B667** 201-241 (2003).

[24] Z.B Kang and J.W Qiu, Phys. Rev. Lett. **103** 172001 (2009).

[25] S.J. Brodsky, P. Hoyer, N. Marchal, S. Peigne, and F. Sannino, Phys. Rev. **D65** 114025 (2002).

[26] E. Iancu, A. Leonidov, and L. McLerran, arXiv:hep-ph/0202270 (2002).

[27] E. Iancu and R. Venugopalan, arXiv:hep-ph/0303204 (2003).

[28] J.J Marian and Y.V. Kovchegov, Prog. Part. Nucl. Phys. **56** 104-231 (2006).

[29] C. Marquet, B.W Xiao, and F. Yuan, Phys. Lett. **B682** 207-211 (2009).

[30] , F. Gelis, E. Iancu, J.J. Marian, and R. Venugopalan, arXiv:hep-ph/1002.0333 (2010) and references therein.

[31] B.W. Xiao and F. Yuan, Phys. Rev. **D82** 114009 (2010).

[32] B.W. Xiao and F.Yuan, Phys. Rev. Lett. **105** 062001 (2010).

[33] J.C. Collins, D.E. Soper, and G.F. Sterman, High Energy Phys. **5** 1-91 (1988).

[34] X.D. Ji, J.P. Ma, and F. Yuan, Phys. Rev. **D71** 034005 (2005).

[35] X.D. Ji, J.P. Ma, and F. Yuan, Phys. Lett. **B597** 299-308 (2004).

[36] J.C. Collins and A. Metz, Phys. Rev. Lett. **93** 252001 (2004).

[37] C.J. Bomhof, P.J. Mulders, and F. Pijlman, Phys. Lett. **B596** 277-286 2004.

[38] J. Collins and J.W. Qiu, Phys. Rev.**D75** 114014 (2007).

[39] W. Vogelsang and F. Yuan, Phys. Rev. **D76** 094013 (2007).

[40] J. Collins, arXiv:hep-ph/0708.4410 (2007).

[41] T.C. Rogers and P.J. Mulders, Phys.Rev. **D81** 094006 (2010).

[42] I.O. Cherednikov and N.G. Stefanis, Phys. Rev. **D77** 094001 (2008).

[43] I.O. Cherednikov and N.G. Stefanis, Nucl. Phys. **B802** 146-179 (2008).

[44] I.O. Cherednikov and N.G. Stefanis, Phys. Rev.**D80** 054008 (2009).

[45] D.W. Sivers, Phys. Rev. **D43** 261-263 (1991).

[46] P. Hagler, B. U. Musch, J.W. Negele, and A. Schafer, Europhys. Lett. **88** 61001 (2009).

[47] B. U. Musch, P. Hagler, J.W. Negele, and A. Schafer, Phys. Rev. D **83**, 094507 (2011); arXiv:hep-lat/1011.1213 (2010).

[48] B. Musch, `https://wiki.bnl.gov/conferences/images/1/1a/Parallel.FD.BernhardMusch.2011`

[49] H. Avakian, A.V. Efremov, P. Schweitzer and F. Yuan, Phys. Rev. D **81**, 074035 (2010).

[50] B.Q. Ma, and I. Schimidt, Phys. Rev. D **58**, 096008 (1998).

[51] B.Q. Ma, I. Schimidt, and J. Soffer, Phys. Lett. B **441**, 461 (1998).

[52] J. She, J. Zhu, and B.Q. Ma, Phys. Rev. **D79** 054008 (2009).

[53] C. Lorce and B. Pasquini, arXiv:1104.565.

[54] C. Lorce and B. Pasquini, arXiv:1106.0139.

[55] S. Meissner, A. Metz, and M. Schlegel, JHEP **0908**, 056 (2009); S. Meissner, A. Metz, M. Schlegel, and K. Goeke JHEP **0808**, 038 (2008).

[56] H. Mkrtchyan *et al.*, Phys. Lett. **B665** 20-25 (2008).

[57] H. Avakian *et al.*, Phys. Rev. Lett. **105** 262002 (2010).

[58] Z. Lu and B-Q Ma, Nucl. Phys. **A741** 200-214 (2004).

[59] M. Anselmino, A. Efremov, A. Kotzinian, and B. Parsamyan, Phys. Rev. **D74** 074015 (2006).

[60] B. Pasquini, S. Cazzaniga, and S. Boffi, Phys. Rev. **D78**, 034025 2008.

[61] C. Bourrely, F. Buccella, and J. Soffer. arXiv:hep-ph/1008.5322 (2010).

[62] Z.-B. Kang *et al.*, Phys. Rev. D **83**, 094001 (2011).

[63] J.C. Collins, Nucl. Phys. **B396**, 61 (1993).

[64] T. Meng, J. Pan, Q. Xie and W. Zhu, Phys. Rev. **D40**, 769 (1989).

[65] M. Anselmino, M. Boglione, and F. Murgia, Phys. Rev. **D60**, 054027 (1999).

[66] M. Burkardt, Phys. Rev. **D69**, 057501 (2004).

[67] A. Airapetian *et al.* (HERMES), Phys. Rev. Lett. **94**, 012002 (2005).

[68] The COMPASS Collaboration, Phys. Rev. Lett. **94**, 202002 (2005).

[69] L.P. Gamberg, G.R. Goldstein, and K.A. Oganessyan, Phys. Rev. **D67** 071504 (2003).

[70] A. Bacchetta, A. Schaefer, and J.J Yang, Phys. Lett. **B578** 109-118 (2004).

[71] L.P. Gamberg, G.R. Goldstein, and M. Schlegel, arXiv:hep-ph/0708.2580 (2007).

[72] A. Bacchetta, F. Conti, and M. Radici, Phys. Rev. **D78** 074010 (2008).

[73] B. Pasquini and F. Yuan, Phys. Rev. **D81** 114013 (2010).

[74] F. Yuan, Phys. Lett. **B575** 45-54 (2003).

[75] D. Amrath, A. Bacchetta, and A. Metz, Phys. Rev.**D71** 114018 (2005).

[76] A. Bacchetta, L.P. Gamberg, G.R. Goldstein, and A. Mukherjee, Phys. Lett. **B659** 234-243 (2008).

[77] A. Metz, Phys. Lett. **B549** 139-145 (2002).

[78] L.P. Gamberg, A. Mukherjee, and P.J. Mulders, Phys. Rev. **D77** 114026 (2008).

[79] G.R. Goldstein and L. Gamberg, arxiv:hep-ph/0209085. Published in Amsterdam ICHEP 452-454 (2003).

[80] Z. Lu and B.Q. Ma, Phys. Rev. **D70** 094044 (2004).

[81] H. Avakian *et al.*, Phys. Rev. **D78** 114024 (2008).

[82] B. Pasquini, S. Cazzaniga, and F. Yuan, Phys. Rev. **D78** 034025 (2008).

[83] S. Boffi, A. V. Efremov, B. Pasquini, and P. Schweitzer, Phys. Rev.**D79** 094012 (2009).

[84] V. Barone, Z. Lu, and B.Q. Ma, Phys. Lett. **B632** 277-281 (2006).

[85] V. Barone, A. Prokudin, and B.Q Ma, Phys. Rev. **D78** 045022 (2008).

[86] M. Anselmino *et al.* Phys. Rev. **D72**, 094007 (2005).

[87] M. Anselmino *et al.* Phys. Rev. **D71** 074006 (2005).

[88] J.C. Collins *et al.*, Phys. Rev. **D73** 094023 (2006).

[89] W. Vogelsang and F. Yuan. Phys. Rev.**D72** 054028 (2005).

[90] M. Anselmino *et al.* Eur. Phys. J. **A39** 89-100 (2009).

[91] A. Airapetian *et al.* Phys. Rev. Lett.**103** 152002 (2009).

[92] M.G. Alekseev *et al.* Phys. Lett. **B692** 240-246 (2010).

[93] M. Anselmino *et al.*, Phys. Rev. D **75**, 054032 (2007).

[94] E.S. Ageev *et al.*, Nucl. Phys. **B765**, 31 (2007).

[95] M. Alekseev *et al.*, Phys. Lett. B **673**, 127 (2009).

[96] K. Abe *et al.*, Phys. Rev. Lett. **96**, 232002 (2006).

[97] M. Anselmino *et al.* Nucl. Phys. Proc. Suppl. **191** 98-107 (2009).

[98] J. Soffer, Phys. Rev. Lett. **74**, 1292 (1995).

[99] X. Qian *eet al.*, arXiv:1106.0363.

[100] R.L. Jaffe and X.D. Ji, Phys. Rev. Lett. **67**, 552 (1991).

[101] V. Barone, A. Drage and P.G. Ratcliffe, Phys. Rept. **359**, 1 (2002).

[102] S. Boffi, A. V. Efremov, B. Pasquini and P. Schweitzer, Phys. Rev. **D79**, 094012 (2009) arXiv:0903.1271.

[103] B.Q. Ma, I. Schmidt and J.J. Yang, Phys. Rev. D **65**, 034010 (2002).

[104] M. Anselmino *et al.*, arXiv:0812.4366.

[105] S. Arnold *et al.*, arXiv:0805.2137.

[106] B. Pasquini and P. Schweitzer, arXiv:1103.5977.

[107] L.P. Gamberg, G.R. Goldstein and M. Schlegel, Phys. Rev. D **77**, 094016 (2008).

[108] H. Gao *et al.*, EPJ-plus **126**, 2 (2011).

[109] JLab proposal PR-12-09-014, PAC34
`http://www.jlab.org/exp_prog/proposals/09/PR12-09-014.pdf`.

[110] JLab proposal E-12-10-006, PAC35
`http://www.jlab.org/exp_prog/proposals/10/PR12-10-006.pdf`.

[111] JLab proposal PR-12-09-12 PAC34, PVDIS proposal.

[112] JLab proposal PR-12-11-007, Spokespersons: J.P. Chen, J, Huang, Y. Qiang, W.B. Yan.

[113] A. Bacchetta, *et al.*, JHEP, 0702, 093 (2007), hep-ph/0611265.

[114] Alessandro Bacchetta, Umberto D'Alesio, Markus Diehl, C. Andy Miller, Phys. Rev. **D70**, 117504 (2004).

[115] M. Anselmino and A. Prokudin, private communications; M. Anselmino, *et al.*, arXiv:0807.0173 (hep-ph).

[116] P. Fabbricatore, *et al.* IEEE TRANSACTIONS ON MAGNETICS VOL **32**, NO. 4, 2210 (1996); R. A. Bell, *et al.*, Nucl. Phys. **B78**, 559 (1999).

[117] D. Crabb *et al.*, Phys. Rev. Lett. **64**, 2627 (1990).

[118] C. Keith *et al.*, NIM A **501**, 327 (2003).

[119] P. Haulte *et al.*, NIM A **356**, 108 (1995).

[120] P. Hautle *et al.* Proceedings of the Workshop on the Polarized Drell-Yan Process, Sante Fe, New Maxico, 2010 (to be published).

[121] D. Crab, private communications.

[122] W. Anderson *et al.*, arXiv:1103.4277v1 [physics.ins-det].

[123] K. Auki *et al.*, Nucl. Instr. and Meth. A 628 (2011) 300.

[124] B. Azmoun et al., IEEE Trans. Nucl. Sci. 56-3 (2009) 1544.

[125] C. Lu, K.T. McDonald, Nucl. Instr. and Meth. A343 (1994) 135-151.

[126] J. She and B.Q. Ma, Phys. Rev. D **83**, 037502 (2011).

[127] W. Vogelsang and F. Yuan, *private communications*.

[128] H. Avakian *et al.*, a new proposal to PAC38 using a transversely polarized HDiced target.